








# A VLBA-uGMRT search for candidate binary black holes: study of six X-shaped radio galaxies with double-peaked emission lines

Biny Sebastian <sup>1</sup>★, Anderson Caproni <sup>2</sup>, Preeti Kharb <sup>3</sup>, A. J. Nayana <sup>4,5</sup>, Arshi Ali,<sup>6</sup> K. Rubinur <sup>7</sup>, Christopher P. O’Dea <sup>1</sup>, Stefi Baum<sup>1</sup> and Sumana Nandi <sup>8</sup>

<sup>1</sup>Department of Physics and Astronomy, University of Manitoba, Winnipeg, MB R3T 2N2, Canada

<sup>2</sup>Núcleo de Astrofísica, Universidade Cidade de São Paulo R. Galvão Bueno 868, Liberdade, São Paulo, SP, 01506-000, Brazil

<sup>3</sup>National Centre for Radio Astrophysics (NCRA) - Tata Institute of Fundamental Research (TIFR), S. P. Pune University Campus, Post Bag 3, Ganeshkhind, 411007 Pune, India

<sup>4</sup>Department of Astronomy, University of California, Berkeley, CA 94720-3411, USA

<sup>5</sup>Indian Institute of Astrophysics, Block II, Koramangala, 560 034 Bangalore, India

<sup>6</sup>Department of Physics, Savitribai Phule Pune University, 411007 Pune, India

<sup>7</sup>Institute of Theoretical Astrophysics, University of Oslo, PO box 1029 Blindern, 0315 OSLO, Norway

<sup>8</sup>Manipal Centre for Natural Sciences, Centre of Excellence, Manipal Academy of Higher Education, Manipal, 576104 Karnataka, India

Accepted 2024 February 20. Received 2024 January 21; in original form 2023 October 1

## ABSTRACT

Identifying methods to discover dual active galactic nucleus (AGN) has proven to be challenging. Several indirect tracers have been explored in the literature, including X/S-shaped radio morphologies and double-peaked (DP) emission lines in the optical spectra. However, the detection rates of confirmed dual AGN candidates from the individual methods remain extremely small. We search for binary black holes (BBH) in a sample of six sources that exhibit both X-shaped radio morphology and DP emission lines using the Very Long Baseline Array (VLBA). Three out of the six sources show dual VLBA compact components, making them strong candidates for BBH sources. In addition, we present deep uGMRT images revealing the exquisite details of the X-shaped wings in three sources. We present a detailed precession modeling analysis of these sources. The black hole separations estimated from the simplistic geodetic precession model are incompatible with those estimated from emission line offsets and the VLBA separations. However, precession induced by a non-coplanar secondary black hole is a feasible mechanism for explaining the observed X-shaped radio morphologies and the black hole separations estimated from other methods. The black hole separations estimated from the double-peaked emission lines agree well with the VLBA compact component separations. Future multifrequency VLBA observations will be critical in ruling out or confirming the BBH scenario in the three galaxies with dual component detections.

**Key words:** galaxies: active – galaxies: jets – quasars: emission lines – radio continuum: galaxies.

## 1 INTRODUCTION

According to the hierarchical galaxy formation scenario, galaxy mergers play a significant role in galaxy dynamics and evolution. It is easy to visually identify systems that are at the early stages and have dual optical cores separated by tens of kpc (Hennawi et al. 2006; Myers et al. 2007; Foreman, Volonteri & Dotti 2009; Darg et al. 2010). However, the dynamics of the later stages of galaxy mergers are hard to study because of several observational limitations. As the cores’ separation becomes less, resolving them individually becomes harder. The obscuration levels due to dust are quite high in the optical cores of merging systems compared to those in isolated galaxies (Liu et al. 2013; Kocevski et al. 2015), making optical identification more difficult. Barnes & Hernquist (1991) have suggested that mergers

result in the funneling of gas to the central supermassive black holes (SMBHs). This gas inflow initiates the activity of the active galactic nucleus (AGN; Hopkins et al. 2005; Hopkins 2008) and could also lead to a starburst near the core. Comerford et al. (2015) have classified SMBH binaries separated by a few kpc during galaxy mergers as dual AGN (DAGN) if both the black holes are active and as ‘offset AGN’ if only one of them is active. Efforts to identify DAGN systems have often seen little success, and so far, there is only a handful of confirmed DAGN reported in the literature (e.g. Deane et al. 2014; Balmaverde et al. 2018; Husemann et al. 2020).

Indirect indicators of binary black holes (BBHs) at the centre of galaxies are double-peaked (DP) emission-lines (Blecha, Loeb & Narayan 2013; Doan et al. 2020; Kharb et al. 2020), periodicity in optical (Bon et al. 2012; Graham et al. 2015; Pihajoki 2016) or radio light curves (O’Neill et al. 2022) and X- or Z-shaped radio sources (Zhang, Dultzin-Hacyan & Wang 2007; Kharb, Lal & Merritt 2017a). Systematic searches to identify DP emission lines in galaxies were

\* E-mail: [biny.sebastian@umanitoba.ca](mailto:biny.sebastian@umanitoba.ca)

carried out by several authors (Liu et al. 2010; Smith et al. 2010; Fu et al. 2012; Ge et al. 2012; Kharb et al. 2021). DP emission lines may occur due to several reasons, including separate narrow-line region (NLR) around two massive black holes at the centre, peculiar gas kinematics in a disc-like narrow line region (Fu & Stockton 2009) and bipolar outflows, which are driven either by AGN radiation or starbursts (Crenshaw et al. 2010) or jet-cloud interaction (Stockton et al. 2007; Rosario et al. 2010; Kharb et al. 2017b, 2019). While the first two reasons are merger-related, the bipolar outflows are not induced by recent merger activity. Hence, the mere presence of these DP emission lines in a galaxy does not guarantee the presence of DAGN. Observations at wavelengths where the nuclei are unobscured, like the X-rays or high-resolution radio observations, are needed to confirm DAGN (Komossa et al. 2003; Hudson et al. 2006; Bianchi et al. 2008). There is only one parsec-scale DAGN detected using Very Long Baseline Interferometric observations (VLBI; Rodriguez et al. 2006). It is worth noting that follow-up high-resolution imaging and spatially resolved spectroscopy of the double-peaked AGN (DPAGN) samples by Shen et al. (2011) and Fu et al. (2011) did not find DAGN in a majority of their sources.

Previous radio studies of DPAGN have mostly relied on high-resolution imaging studies to resolve the dual radio cores (Tingay & Wayth 2011; Müller-Sánchez et al. 2015). The large-scale radio morphologies for a sample of DPAGN have not been explored in detail so far. There are several individual source studies where DPAGN are also hosted by X/S shaped radio galaxies (Zhang, Dultzin-Hacyan & Wang 2007; Wang et al. 2009; Rubinur et al. 2017; Nandi et al. 2021). Three major formation mechanisms for X/S-shaped radio sources have been proposed in the literature. These include realignment of the jets (Ekers et al. 1978; Rees 1978; Klein et al. 1995), backflow diversion (Leahy & Williams 1984) and twin AGN (Lal & Rao 2005, 2007; Lal et al. 2019). The realignment of jets is believed to occur either due to the precession of the jet or a spin flip of the SMBH powering the jets, which in turn is induced by coalescence of a BBH (Rottmann 2001; Dennett-Thorpe et al. 2002; Merritt & Ekers 2002; Zier 2005).

The precession of jets from BBHs on galactic scales is known to exist. This precession occurs due to the gravitational influence of the second member in the binary (see for example, Fabrika 2004). Similarly, in the case of extragalactic jets, the precession has been attributed to the presence of a BBH pair at the centre of the galaxy (Begelman, Blandford & Rees 1980). These black holes are remnants of two merged galaxies, each initially having a SMBH at the centre. Yet another explanation for jets' precession is the warping of accretion discs (Liu 2004).

BBH scenario forms one among several possible explanations for the appearance of both DP emission lines and cross-symmetric morphology. While isolated cases of DPAGN hosting X or S-shaped radio galaxies were reported in the past, a systematic study of a comprehensive sample has not yet been done. If mergers or BBHs lead to both the X-shaped radio morphology and the DAGN formed from the merger leads to the DP emission features, we expect that a sample of DPAGN with X/S-shaped radio morphology should improve the probability of the detection of dual DAGN.

The expected black hole separations for a sample of sources selected on the basis of these two criteria are only a few parsecs. Hence, Very Long Baseline Array (VLBA) proves to be the ideal telescope to zoom into the centres of such merger systems. Begelman, Blandford & Rees (1980) have shown that a DAGN would remain at  $> 1$  kpc separation before getting closer for at least 100 Myr. Afterward, the time-scales of evolution to  $\sim 1$  pc separation via the scattering of stars in the nucleus could be anywhere between  $10^8$  and

$10^9$  yr (the loss-cone problem). Such large time-scales mean that we need not see merger signatures surrounding the host galaxy, such as tidal features, as they are usually detectable only up to 200–400 Myr (Lotz et al. 2010). Hence, detecting and confirming BBHs at  $\sim$ pc scale separations is extremely hard. Fig. 1 from Chen et al. (2022) illustrate this rarity of double quasars reported in the literature below a separation of 1 kpc. However, the double peaks in optical spectra arising from rotating discs due to major mergers arise around 1 Gyr after the final coalescence (Maschmann et al. 2023) and could be a better tracer of pc-scale binaries.

In this paper, we have studied a sample of six galaxies possessing both a cross-symmetric radio morphology and double-peaked emission lines in their optical spectra using the VLBA and upgraded Giant Metrewave Radio Observations (uGMRT). The paper tests whether our sample selection criteria are robust for identifying DAGN. The paper is organized as follows. We describe our sample selection in Section 2 and provide the observational details and the data analysis in Section 3. In Section 4, we present the results of various analyses on our sample sources. We discuss the implications of our results in Section 5 and finally summarize our conclusions in Section 6.

## 2 SAMPLE SELECTION

Ge et al. (2012) had searched for DP emission lines in the SDSS DR7 spectra (Abazajian et al. 2009) of a sample of 920 000 galaxies. They had visually inspected a sub-sample of 42 927 candidate DP emission line galaxies, which possessed two Gaussian components in their emission spectra. They presented a final sample of 3030 DP narrow-emission line galaxies, ensuring the presence of a clear trough between two narrow emission lines. We cross-matched the location of the optical host galaxies from this complete sample of 3030 DP narrow emission-lines galaxies listed in Ge et al. (2012) with the VLA FIRST survey catalogue (Becker, White & Helfand 1995) images within a distance of 1 arcmin. We then visually inspected the radio images of the resulting 643 cross-matches using VLA FIRST, TGSS (Intema et al. 2017), and NVSS surveys and found that 30 sources showed extended radio emission. Out of these 30, four showed cross-symmetric morphology. The large-scale radio structure in J1328 + 27 has already been studied by Nandi et al. (2017). We obtained uGMRT observations for the three remaining sources, viz, B2 1059+29, 4C + 32.25, and 4C 61.23, at Band 3 (250–300 MHz) and Band 5 (1000–1450 MHz).

In addition to the above sources, Wang et al. (2009) had reported that 3C 223.1, and J1430+54 show DP narrow emission lines and X-shaped radio morphology. Hence, we observed all these six potential BBH candidates with the VLBA to uncover DAGN. We obtained 5 GHz VLBA observations for the four sources, including the three sources that did not have any phase-referenced VLBA archival data. We observed the two sources that already had archival VLBA data, namely, 4C +32.25 and 4C +61.23 at 15 GHz. A detailed analysis of the VLBA observations of J1328 + 2752 has already been presented by Nandi et al. (2021). We summarize the results of the remaining sources in the current paper.

## 3 OBSERVATIONS AND DATA ANALYSIS

### 3.1 VLBA observations: 5 and 15 GHz

Data were acquired with nine antennas of the VLBA in a phase-referencing mode on 2018 August 11 at 4.85 GHz and 2018 August 13 at 15.13 GHz (Project IDs: BS267B and BS267A, respectively). Pie Town (PT) did not participate in the experiment. The total

**Table 1.** Sources and observed properties.

VLBA observations							
Source name	Alternate name	Redshift (z)	Observation date	$\nu_{\text{cen}}$ (GHz)	Beam, PA (mas, °)	Image peak flux density (mJy)	Image rms (mJy per beam)
4C + 32.25	J0831 + 3219	0.05121	2018 Aug 13	15.26	$1.07 \times 0.49, -4.17$	0.6	0.06
3C 223.1	J0941 + 3944	0.10747	2018 Aug 11	4.98	$3.46 \times 1.62, 15.56$	2.9	0.02
B2 1059 + 29	J1102 + 2907	0.10598	2018 Aug 11	4.98	$3.4 \times 1.53, 1.35$	0.1	0.02
4C + 61.23	J1137 + 6120	0.11110	2018 Aug 13	15.26	$1.06 \times 0.52, 29.18$	0.4	0.06
J1328 + 27	J1328 + 2752	0.09	2018 Aug 11	4.98	$3.44 \times 1.52, -0.34$	0.3	0.02
J1430 + 52	J1430 + 5217	0.3671	2018 Aug 11	4.98	$3.56 \times 1.51, -15.4$	4.9	0.02
uGMRT observations							
Source name	Observation date	$\nu_{\text{cen}}$ (MHz)	Beam, PA (arcsec, °)	Image peak flux density (mJy per beam)	Image r.m.s (mJy per beam)		
4C + 32.25	2017 Nov 04	Band 3 (250–500)	$12.2 \times 7.7, 80.42$	123.9	0.08		
	2017 Oct 28	Band 5 (1000–1450)	$6.2 \times 3.9, 64.6$	26.5	0.15		
B2 1059 + 29	2017 Oct 27	Band 3 (250–500)	$12.3 \times 8.5, 49.03$	85.5	0.76		
	2017 Oct 28	Band 5 (1000–1450)	$5.1 \times 2.6, 76.6$	21.2	0.17		
4C + 61.23	2017 Nov 04	Band 3 (250–500)	$12.2 \times 8.1, 49.03$	146.3	0.19		
	2017 Oct 28	Band 5 (1000–1450)	$4.0 \times 3.4, -48.41$	32.3	0.07		

**Table 2.** The estimations from the equipartition assumption:  $L_{\text{rad}}, B_{\text{min}}, \text{Age}$ .

Source	Reference Frequency (GHz)	Flux <sub>Reffreq</sub> (Jy)	$\alpha$	$L_{\text{rad}}$ ( $\text{erg s}^{-1}$ )	$B_{\text{min}}$ ( $\mu\text{G}$ )	Age (Myr)
4C 32.25 (primary)	1.4	$1.69 \pm 0.16$	$-0.43 \pm 0.05$	$(4.91 \pm 0.97) \times 10^{42}$	$2.17 \pm 0.12$	$51.10 \pm 1.44$
4C 32.25 (secondary)	1.4	$0.26 \pm 0.03$	$-0.55 \pm 0.08$	$(1.09 \pm 0.26) \times 10^{41}$	$0.40 \pm 0.02$	$22.15 \pm 0.77$
4C 61.23 (primary)	1.25	$0.91 \pm 0.09$	$-0.58 \pm 0.08$	$(1.14 \pm 0.24) \times 10^{42}$	$1.72 \pm 0.10$	$37.52 \pm 1.14$
4C 61.23 (secondary)	1.25	$0.38 \pm 0.03$	$-0.52 \pm 0.06$	$(1.36 \pm 0.23) \times 10^{42}$	$1.16 \pm 0.05$	$30.89 \pm 0.74$
B2 1059 + 29	1.25	$0.13 \pm 0.13$	$-0.42 \pm 0.05$	$(2.29 \pm 0.37) \times 10^{42}$	$2.93 \pm 0.13$	$50.01 \pm 1.16$

bandwidth of the data was 256 MHz. The calibrators DA193 and J1800+3848 were used as the fringe finders for the experiment. The phase calibrators used were J0819+3226, J1128+5925 at 15 GHz, and J1333+2725, J0934+3926, J1103+3014, J1437+5112 at 5 GHz. The data were reduced using the VLBARUN data-reduction pipeline with appropriate parameters inside AIPS, with Los Alamos (LA) as the reference antenna. Five sources, viz. 4C 32.25 (at 15 GHz) and J1328+2752, 3C 223.1, J1430+5217, and B2 1059 + 29 (at 5 GHz) were detected.

### 3.2 uGMRT observations: Band 3 and Band 5

Details of the observations of three sources that were observed using the uGMRT at Band 3 and Band 5 are provided in Table 1. The data analysis used the uGMRT data analysis pipeline `aipssc-riptwriter`.<sup>1</sup> It uses both AIPS and CASA tasks to carry out the initial editing and flagging of bad data. The pipeline calibrates the data using standard procedures in AIPS. The target source is split out from this data set while averaging several channels. The initial few rounds of imaging and phase self-calibration are done in AIPS, after which the final imaging is done using the MT-MFS algorithm (Rau & Cornwell 2011) that is available in CASA. The GMRT images of the three galaxies in Bands 3 and 5 are shown in Figs 2 and 3. We have also provided the details of the flux measurements and spectral index values for the various sources in Table 2.

### 3.3 SDSS optical spectral modeling

The modeling of the optical spectra for all sources except J1430 + 5217 was already carried out and presented by Ge et al. (2012) and Wang et al. (2009). While Wang et al. (2009; see Section 4.3) specifies the presence of double-peaked emission lines in the SDSS spectra of J1430+5217, they do not provide the emission line modeling results for this galaxy. Hence, in this paper, we perform spectral modeling and the double Gaussian fitting for the emission lines in J1430 + 5217. We used the SDSS spectra with wavelength coverage from  $\sim 4000$ – $9000 \text{ \AA}$ .

To perform the spectral fitting for J1430 + 5217, we have used the open-source PYTHON code Bayesian AGN Decomposition Analysis for SDSS Spectra pipeline BADASS3<sup>2</sup> (Sexton et al. 2021). BADASS3 performs modeling for various components (e.g. power-law continuum, stellar line-of-sight velocity distribution, emission lines, and potential outflows). For the analysis presented in this paper, we only require the emission line parameters of [O III] and  $H\beta$  line. Hence, we restricted the wavelength range to 4800–5050  $\text{\AA}$ . We used the empirical stellar template Indo-US (Valdes et al. 2004) to fit the continuum emission. The BADASS3 pipeline iteratively refines the estimated parameters and components until the best fit to the original data is achieved. We use the redshift of the source to determine the rest frame velocity of the galaxy. For J 1430 + 5217, the peak of the absorption lines is consistent with the rest frame velocity within the error bar. For the rest of the sources, Ge et al. (2012) use absorption lines to estimate the systemic velocity.

<sup>1</sup><https://github.com/binysebastian/aipssc-riptwriter><sup>2</sup><https://github.com/remingtonsexton/BADASS3>

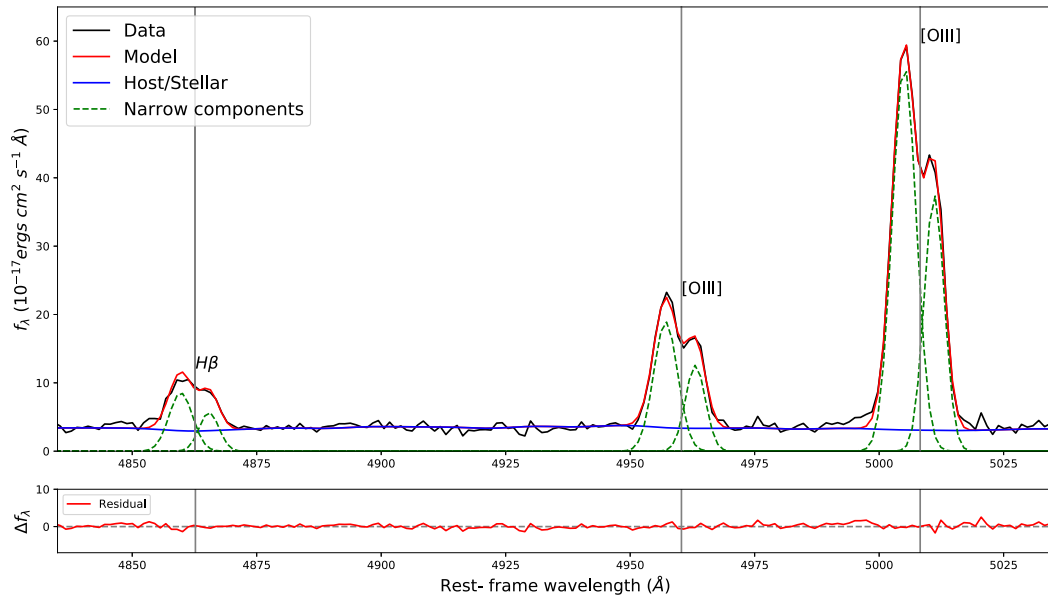


**Figure 1.** Spectral fitting of J1430+5217 for H $\beta$  + [O III] complex lines using the BADASS (Sexton et al. 2021). The emission lines have been fitted using double Gaussian profiles. The solid red line represents the overall model obtained by fitting, the solid blue line represents the combined continuum level, which includes both the host-galaxy and AGN continuum contributions, and the dashed green lines correspond to the recognized narrow emission lines considered in the fitting process. The vertical solid line corresponds to the rest frame wavelength of the emission lines.

**Table 3.** Black hole mass estimates from emission lines.

Source name	$\Delta v_b$ (km s $^{-1}$ )	$\Delta v_r$ (km s $^{-1}$ )	$\sigma_*$ (km s $^{-1}$ )	$\sigma_{b,[OIII]}$ (km s $^{-1}$ )	$\sigma_{r,[OIII]}$ (km s $^{-1}$ )	$\log(M_{BH2})$ ( $M_\odot$ )	$\log(M_{BH1})$ ( $M_\odot$ )	$\log(M_{tot,\sigma_*})$ ( $M_\odot$ )	$\log(M_{tot,sum})$ ( $M_\odot$ )	$M_{BH}$ ratio $\frac{v_r}{v_b}$	$M_{BH}$ ratio $\frac{M_{BH2}}{M_{BH1}}$
(1)	(2)	(3)	(4)	(5)	(6)	(7)	(8)	(9)	(10)	(11)	(12)
4C + 32.25	$-211.0 \pm 9.30$	$107.2 \pm 12.80$	$222.7 \pm 5.3$	$105.2 \pm 7.6$	$165.6 \pm 10.5$	$7.0 \pm 1.4$	$7.7 \pm 1.6$	$8.32 \pm 0.07$	$7.8 \pm 1.$	$0.50 \pm 0.06$	$0.19 \pm 0.09$
3C 223.1	$-148.5 \pm 5.00$	$131.2 \pm 3.90$	$200.2 \pm 7$	$112 \pm 2.9$	$121.3 \pm 2.4$	$7.1 \pm 1.4$	$7.2 \pm 1.5$	$8.13 \pm 0.09$	$7.5 \pm 1.5$	$0.88 \pm 0.04$	$0.79 \pm 0.1$
B2 1059 + 29	$-167.9 \pm 5.50$	$249.3 \pm 5.80$	$215.2 \pm 8.0$	$164.2 \pm 5.3$	$124.5 \pm 5.1$	$7.7 \pm 1.6$	$7.3 \pm 1.5$	$8.26 \pm 0.09$	$7.8 \pm 1.5$	$1.48 \pm 0.06$	$2.51 \pm 0.8$
4C + 61.23	$-39.2 \pm 1.90$	$261.4 \pm 2.10$	$200.3 \pm 11.4$	$139.6 \pm 1.1$	$102.6 \pm 1.2$	$7.4 \pm 1.5$	$6.9 \pm 1.4$	$8.13 \pm 0.12$	$7.6 \pm 1.5$	$6.66 \pm 0.32$	$3.16 \pm 0.7$
J1430 + 5217 <sup>a</sup>	$-191.7 \pm 5.46$	$169. \pm 7.14$	$251.6 \pm 22.0$	$132.5 \pm 4.8$	$105.2 \pm 6.25$	$7.4 \pm 1.5$	$7.0 \pm 1.4$	$8.53 \pm 0.17$	$7.5 \pm 1.5$	$0.88 \pm 0.04$	$2.5 \pm 0.7$

Column 1: Source names. J1328 + 2758 is not presented in this paper, and we refer the reader to Nandi et al. (2021) for details on this source. Columns 2 and 3: Velocity offset of the blue and the red component from the systemic velocity. Column 4: Stellar velocity dispersion. Column 5: Blue narrow line component velocity dispersion. Column 6: Red narrow line component velocity dispersion. Columns 7 and 8: Logarithm of black hole mass for the blue and red components, respectively (see Section 4.4 for more details). Column 9: Logarithm of the total black hole mass from  $M-\sigma_*$  relation. Column 10: Logarithm of the total black hole mass estimated as a sum of the individual black holes. <sup>a</sup>The emission line properties for all sources except J1430 + 5217 were obtained from Ge et al. (2012) and Wang et al. (2009). We have completed the double Gaussian model fitting for J1430 + 5217 and presented the details in Section 3.3. Column 11: Black hole mass ratio estimated using the ratio  $v_r/v_b$ . Here,  $v_r$  and  $v_b$  represent the offset of the emission lines' peak from the galaxy's systemic velocity. Column 12: Black hole mass ratio estimated directly using columns 7 and 8. Since the black hole masses depend on the full width at half-maximum of the individual line profiles, this estimation method is independent of the method used for Column 11.

BADASS3 treats multiple line components as outflows, and hence, we model the emission lines as a combination of narrow-line and outflow components. We assume Gaussian profiles for both these components. Fig. 1 shows the raw spectra, the model, and individual components, including the stellar continuum and the multiple Gaussian narrow emission lines. Even though we modeled the emission lines using a narrow + outflowing component, neither of these components seems to be centred around the systemic velocity of the host galaxy, pointing to the existence of double-peaked emission lines. We have tabulated the results of this emission line fitting required for the analysis in this paper in Table 3.

## 4 RESULTS

We describe the results of the uGMRT and VLBA observations below. We present the results for individual sources first, followed by a global analysis.

### 4.1 Radio morphology with the uGMRT

#### 4.1.1 4C 32.25

Our total intensity maps of 4C 32.25 at 400 and 1250 MHz are presented in Fig. 2. The high resolution offered by uGMRT at low frequencies and enhanced sensitivity with the bandwidth upgrade enabled us to map the detailed structure of the diffuse emission in both the primary and the secondary lobes. We can distinctly spot the core, the jet towards the east, and the counterjet towards the western side, as inferred from the brightness ratio. The jets are not perfectly linear and possess a significant curvature. Our maps also reveal the extended nature of both hotspots, a feature not witnessed commonly in radio galaxies. The eastern hotspot has a linear extension towards the northwest, aligned almost at right angles to the jet. The non-linearity of the jets, the extension of the hotspots, and the presence of secondary lobes in the source vouch for a dynamic model for the X-shape in the source.

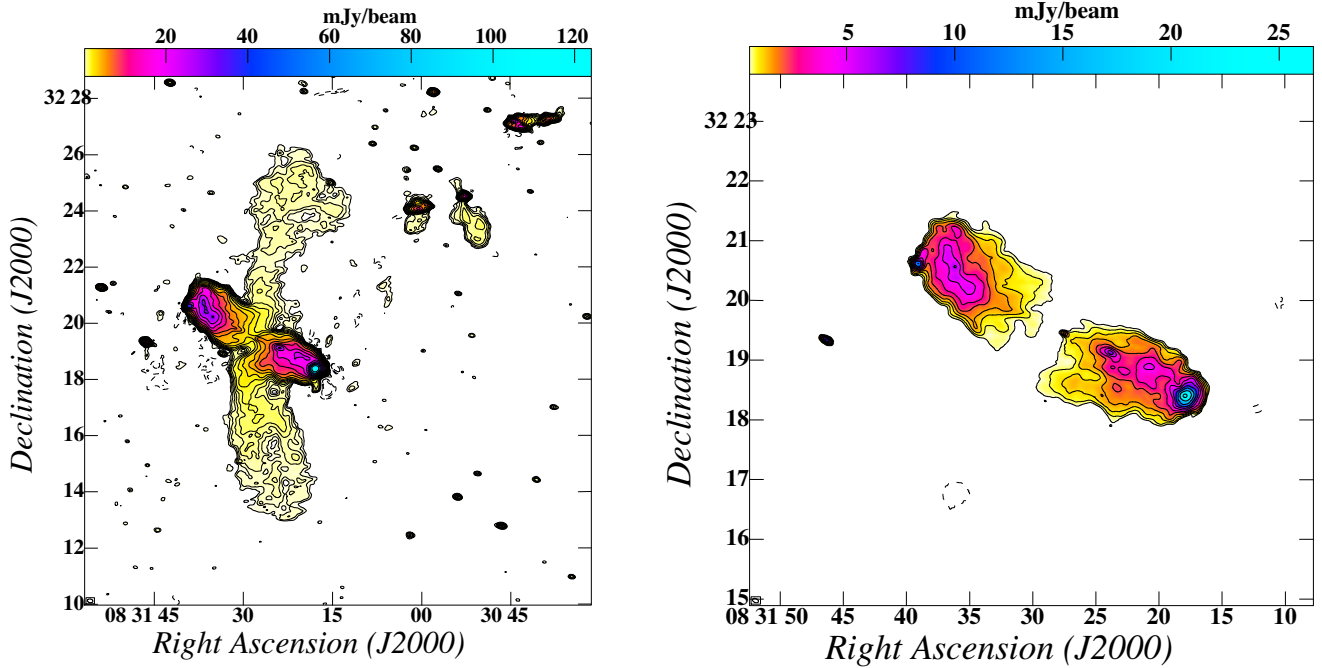


**Figure 2.** Left: uGMRT image of 4C+32.25 at 400 MHz. Contour levels are  $0.23 \text{ mJy} \times (-2, -1.4, -1, 1, 1.4, \dots)$ . Right: uGMRT image of 4C + 32.25 at 1250 MHz. Contour levels are  $0.67 \text{ mJy} \times (-2, -1.4, -1, 1, 1.4, \dots)$ . The image resolution and rms are provided in Table 1. The beam full width at half-maximum (FWHM) is shown at the bottom left corner of the images.

#### 4.1.2 B2 1059 + 29

B2 1059 + 29 is at a redshift of  $z = 0.106$ . The SDSS spectrum of the source shows double-peaked [O III] lines. The Legacy Survey image of B2 1059 + 29 shows tidal features suggesting a past merger event. The source appears to possess a rotational symmetry in the low-resolution images. The detailed structure of the source is conspicuous in our higher-resolution images. The jet direction is seen to be changing continuously throughout the length of the jet. Very close to the core, there is an elongation of the jet in the north-south direction. This is consistent with the jet seen using the VLA high-resolution image (Rubinur, Das & Kharb 2019), which is aligned along the north-south direction. The jet seems to change its alignment on larger scales, and the primary jet, as seen in our L-band images, is aligned along the northeast-southwest (NE-SW) direction. The jet seems to change its direction resulting in the formation of an S-shaped structure.

#### 4.1.3 4C 61.23

4C + 61.23 was classified as an Fanaroff Riley (FR) -II radio galaxy using the 5 GHz VLA image (Lara et al. 2001). The GMRT maps at both bands show clear ‘X’ shaped morphology of this source. The primary and secondary lobes are visible. From visual inspection, it looks like there is a continuity in the emission from the brighter lobes to the fainter ones.

## 4.2 Dual compact components in VLBA: Candidate BBHs

Three of the six sources in our sample show evidence for dual radio compact components in at least one frequency image with the VLBA. All three sources therefore are possible BBH candidates that need to be confirmed with follow-up observations. We do not detect a second component in the rest of the three sources, namely, 3C 223.1,

J1430 + 52, and 4C 32.25. However, 3C 223.1 and 4C 32.35 show extended pc scale morphology, which might be due to the core-jet system. We discuss the VLBA morphology of the three sources exhibiting dual-components below.

#### 4.2.1 B2 1059 + 29

This source shows two close, faint, compact components in the VLBA image (see Fig. 4). The central point-source spectrum estimated using our uGMRT images at 400 and 1250 MHz is steep ( $\alpha \sim -0.8$ ), diminishing the likelihood of the BBH scenario. Since the central point-source spectrum is steep, the extended structure seen in the VLBA image might likely be jet-related, and the source morphology closely resembles a compact symmetric object (CSO). If accurate, the misalignment of the inner double with the outer lobe will provide clues to distinguish between the backflow and realignment models for X-shaped sources. However, without adequate follow-up observations, it is impossible to rule out the BBH scenario at this stage. The candidate BBH separation is 4.3 pc, as inferred from the angular separation and the galaxy’s redshift. Note that the distinction between two separate components in B2 1059 + 29 is not very obvious and could also be a result of imaging artifacts.

#### 4.2.2 J1328 + 2752

J1328 + 2752 is another source that shows dual VLBI components [see Nandi et al. (2021) for a detailed discussion of this source]. However, the DAGN nature has not yet been confirmed due to the lack of spectral index information. Nandi et al. (2017) have pointed out that the source possesses a flat spectrum core based on its VLA image. We must obtain near-simultaneous observations at dual frequencies to confirm the nature of both the VLBA components. The projected

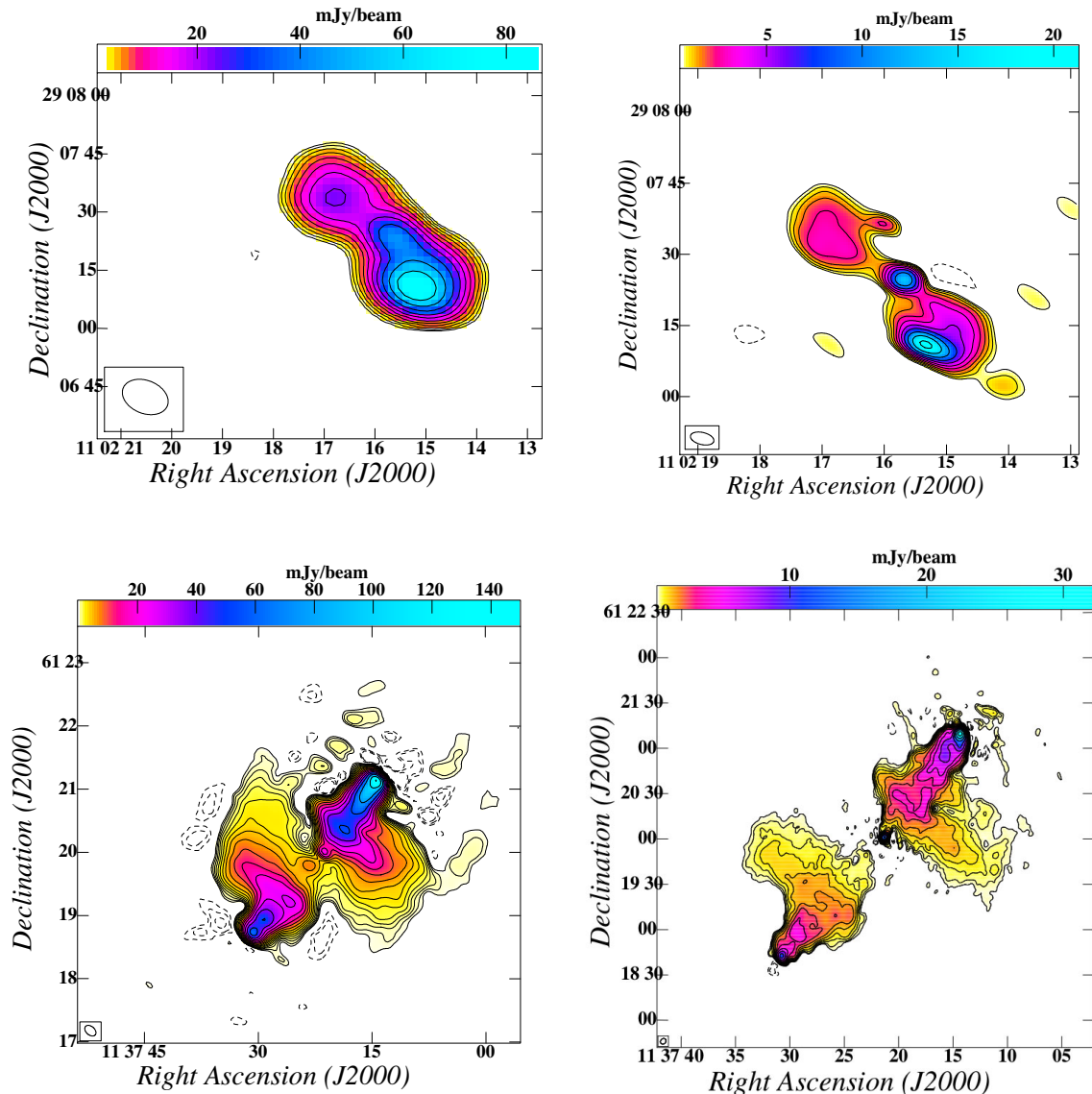


**Figure 3.** Top left: uGMRT images of B2 1059+29 at 400 MHz. Contour levels are  $2 \text{ mJy} \times (-2, -1.4, -1, 1, 1.4, \dots)$ . Top right: uGMRT image of B2 1059+29 at 1250 MHz. Contour levels shown are  $0.6 \text{ mJy} \times (-2, -1.4, -1, 1, 1.4, \dots)$ . Bottom left: uGMRT image of 4C+61.23 at 400 MHz. Contour levels are  $0.41 \text{ mJy} \times (-2, -1.4, -1, 1, 1.4, \dots)$ . Bottom right: uGMRT image of 4C + 61.23 at 1250 MHz. Contour levels are  $0.31 \text{ mJy} \times (-2, -1.4, -1, 1, 1.4, \dots)$ . The image resolution and rms are provided in Table 1. The beam FWHM is shown at the bottom left corner of the images.

separation between the two components is equal to 6 pc (Nandi et al. 2021).

#### 4.2.3 4C + 61.23

Liu et al. (2018) have presented the 8.4 GHz VLBA image of this AGN, which shows a double structure. Our follow-up observations at 15 GHz are similar to the 8.4 GHz image but suffer from low SNR. One of the dual VLBI components appears extended and might be a core-jet structure by itself, while the south-eastern component might be another AGN core. It is also possible that either component is an AGN core, and the rest of the emission is jet-related. Our follow-up uGMRT observations show a dimmed core at the 400 MHz image compared to L-band ( $\alpha \sim -0.25$ ). The angular separation between the dual VLBA components would correspond to a projected distance of 4.6 pc at the source’s redshift.

#### 4.3 Radio spectral index analysis

As our sample galaxies have multiband radio data, we have calculated the spectral indices and used those to obtain the minimum magnetic field and approximate ages for both the primary and secondary lobes. First, we mask the nuclear emission using the circular aperture from *photutils*<sup>3</sup> then we estimated the flux densities from primary and secondary jet (by interactively defining regions using CASA). The errors in flux densities are calculated using  $\sqrt{(\sigma_{\text{rms}} \cdot \sqrt{N_b})^2 + (\sigma_p \cdot S)^2}$  (Kale, Shende & Parekh 2019) where  $\sigma_{\text{rms}}$  is the rms noise of the maps,  $N_b$  is the number of beams inside the selected regions,  $S$  is the sources flux density, and  $\sigma_p$  is the absolute flux density scale error in percentage which is assumed to be 0.1 (conservative for the

<sup>3</sup><https://photutils.readthedocs.io/en/stable/aperture.html>

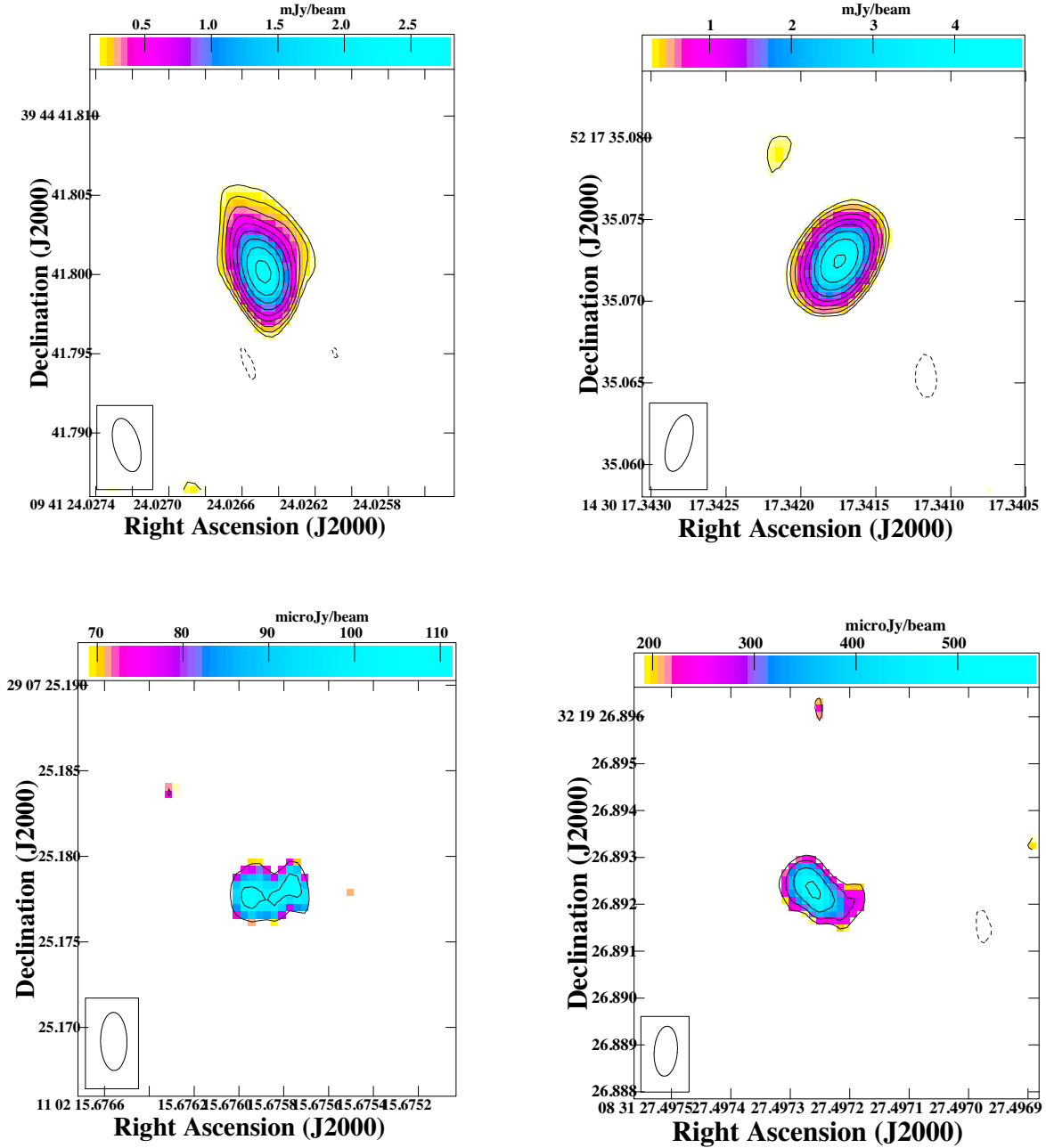


**Figure 4.** Top left: 5 GHz VLBA image of 3C223.1. Top right: 5 GHz VLBA image of J1430+52. Bottom left: 5 GHz VLBA image of B2 1059 + 059. Bottom right: 15 GHz VLBA image of 4C32.25. The image rms and resolution are provided in Table 1. The beam FWHM is shown at the bottom left corner of the images.

GMRT, VLA, and VLBA). We assume that the total energy of the synchrotron emitting plasma in the jet is close to the equipartition of the magnetic field and the energy in particles (Burbidge 1959). Using the following expressions from O’Dea & Owen (1987) we calculate the total luminosity ( $L_{\text{rad}}$ ) and minimum magnetic field ( $B_{\text{min}}$ ),

$$L_{\text{rad}} = 1.2 \times 10^{27} D_L^2 S_0 \frac{(v_u^{1+\alpha} - v_l^{1+\alpha})}{v_0^\alpha (1+\alpha)(1+z)^{1+\alpha}} \quad (1)$$

$$B_{\text{min}} = \left[ \frac{2\pi(1+k)c_{12}L_{\text{rad}}}{(V\phi)} \right]^{2/7} \quad (2)$$

Here,  $D_L$  is the luminosity distance in Mpc, and  $S_0$  is the total flux in Jy at the frequency  $\nu_0$  in Hz. We have taken the radio

spectrum range from 10 MHz ( $\nu_l$ ) to 100 GHz ( $\nu_u$ ). Assuming that the relativistic electron and proton have a similar energy, we have set the ratio  $k = 1$ , and the constant  $c_{12}$  is obtained from Pacholczyk (1970) depending on the calculated spectral index values and the frequency cutoffs. The jets are assumed to have cylindrical symmetry, and hence their volumes are calculated as  $V = \pi(w/2)^2 l$  where  $w$  is the width in kpc, and  $l$  is the length of the jet in kpc. The jets are filled with relativistic particles and magnetic fields uniformly, i.e.  $\phi = 1$ .

Next, we estimated the lifetime of electrons in the radio jet using the following relation from van der Laan & Perola (1969) where the electrons are losing energy via synchrotron as well as inverse-Compton emission mechanisms due to CMB (cosmic microwave

**Table 4.** Model parameters used to generate the precession helices shown in Fig. 5.

Source	$\iota$	$P_{\text{prec, obs}}$ (Myr)	$\beta$	$\eta_0$ (deg)	$\phi_0$ (deg)	$\varphi_0$ (deg)	$\tau_{0, s}$
4C + 32.25	-1	87.5	0.033	105.0	31.0	29.0	0.0
B2 1059 + 29 (NE jet)	-1	48.0	0.120	95.0	7.0	6.9	0.69
B2 1059 + 29 (SW jet)	-1	96.0	0.016	279.0	26.0	25.9	0.69
4C + 61.23	-1	6.5	0.193	106.0	30.0	17.0	0.95
3C 223.1	1	8.0	0.090	327.0	20.0	15.0	0.32
J1328 + 2758	1	4.8	0.170	343.0	40.0	17.0	0.88
J1430 + 52	1	5.0	0.250	63.0	26.0	14.0	0.54

background) photons:

$$t = \frac{2.6 \times 10^4 B_{\text{min}}^{1/2}}{(B_{\text{min}}^2 + B_R)^2 [(1+z)v_b]^{1/2}}, \quad (3)$$

where  $B_{\text{min}}$  is the minimum magnetic field calculated above, assuming the equipartition assumption,  $v_b$  is the break frequency, and  $B_R$  is the magnetic field equivalent to the radiation via IC-CMB. The estimated electron age and other parameters in this section are given in Table 2.

The primary lobe is steeper than the secondary lobe in 4C 61.23. However, the difference is smaller than the quoted error bars. The spectral ages of the primary lobes appear to be larger than the secondary lobes in both 4C 61.23, and 4C 32.25. According to the most well-accepted models, including backflow diversion and precessional models, the primary lobes are expected to comprise the younger relativistic plasma population. This discrepancy could be because of the assumptions involved in calculating spectral age. Since we only have data at two frequencies, we assumed the highest frequency of our observations to be the break frequency. Moreover, the relativistic plasma need not follow the equipartition assumption. Hence, we abstain from making further comments in the absence of data at higher frequencies.

#### 4.4 BH mass estimates

We estimate the total black hole mass using the  $M-\sigma_*$  relation (Ferrarese & Merritt 2000; Gebhardt et al. 2000; Tremaine et al. 2002).

$$M_{\text{BH}} = 10^{8.13 \pm 0.06} \left( \frac{\sigma}{200 \text{ km s}^{-1}} \right)^{4.02 \pm 0.32} M_{\odot} \quad (4)$$

The velocity dispersion of the target galaxies is estimated by fitting the absorption line spectra via direct pixel method (Ge et al. 2012). We have tabulated the stellar velocity dispersion values and the BH masses for the five sources in our sample in Table 3. The ratio of the masses of individual black holes can be approximately determined following Kepler's law by the below equation.

$$\frac{M_{\text{BH1}}}{M_{\text{BH2}}} \sim \frac{v_2}{v_1} \quad (5)$$

Here  $v_1$  and  $v_2$  are the line of sight rotation velocity of each peak. The BH mass ratios are  $M_{\text{BH1}}/M_{\text{BH2}} \sim 1.97, 0.67,$  and  $1.36$  for galaxies 4C+32.25, B2 1059+29, and 4C + 61.23, respectively.

Nelson (2000) studied the relationship between the [O III]  $\lambda 5007$  line widths and the black hole masses for AGN, under the assumption that the forbidden line kinematics is determined by the gravitational influence of the galaxy bulge. They find a moderately strong

correlation between the [O III] line widths and black hole masses.

$$\log_{10}(M_{\text{BH}}) = (3.7 \pm 0.7) \log_{10} \left( \frac{\text{FWHM}[\text{O III}]}{2.35} \right) - (0.5 \pm 0.1) \quad (6)$$

We use the above equation to determine the individual black hole masses, assuming that separate NLR regions produce these lines. The full width at half-maximum of the blueshifted and redshifted [O III] narrow emission lines were obtained from Ge et al. (2012). The individual black hole masses obtained using equation (6) and the total mass estimated from both the relations match within error bars (see Table 3). The precessional period estimated from our radio data can now be applied to obtain the separation between the two black holes, assuming that a DAGN at the centre is responsible for both the double-peaked emission lines and the X-shaped radio morphology.

#### 4.5 Precession modeling

We applied a precession model to the jet/counter-jet of the radio sources of our sample. In summary, this model assumes that the jet propagates with a constant speed  $v = \beta c$  ( $0 < \beta < 1$ ), making an instantaneous angle  $\phi$  with the line of sight. Due to precession, jet/counter-jet will form an apparent cone-like structure with a semi-aperture angle  $\varphi_0$ . The precession cone axis makes a viewing angle  $\phi_0$ , and it is projected on the sky plane with a position angle  $\eta_0$  (measured positively from North to East direction). The initial jet direction is reached after an elapsed time  $P_{\text{prec, obs}}$ , the precession period measured at the observer's reference frame. The two additional free parameters are the sense of precession,  $\iota$  ( $= 1$  for clockwise sense and  $\iota = -1$  for counter-clockwise sense), and the precession phase  $\tau_{0, s}$ . For further details on the kinematic precession model adopted in this work, see e.g. Caproni, Monteiro & Abraham (2009).

We proceeded with a systematic search for the most suitable precession model parameters for each source of our sample, except for J1328 + 2758, for which the jet precession analysis was previously done in Nandi et al. (2021). These parameters are listed in Table 4, while the precession helices generated from these models are shown in Fig. 5. The precession helices are produced under the assumption that the jet and counter-jet are formed by plasma elements ejected steadily from the core during a certain interval and with a constant speed (e.g. Nandi et al. 2021). A given plasma element ejected at a time  $t_{\text{ej}}$  and with a proper motion  $\mu(t_{\text{ej}})$  will present right ascension and declination offsets from the core at a time  $t_{\text{obs}} (\geq t_{\text{ej}})$ ,  $\Delta RA(t_{\text{obs}})$ , and  $\Delta DEC(t_{\text{obs}})$ , respectively, calculated from (e.g. Caproni & Abraham 2004; Caproni, Monteiro & Abraham 2009):

$$\Delta RA(t_{\text{obs}}) = \pm \mu(t_{\text{ej}}) \sin [\eta(t_{\text{ej}})] \Delta t_{\text{obs}}, \quad (7)$$

$$\Delta DEC(t_{\text{obs}}) = \pm \mu(t_{\text{ej}}) \cos [\eta(t_{\text{ej}})] \Delta t_{\text{obs}}, \quad (8)$$



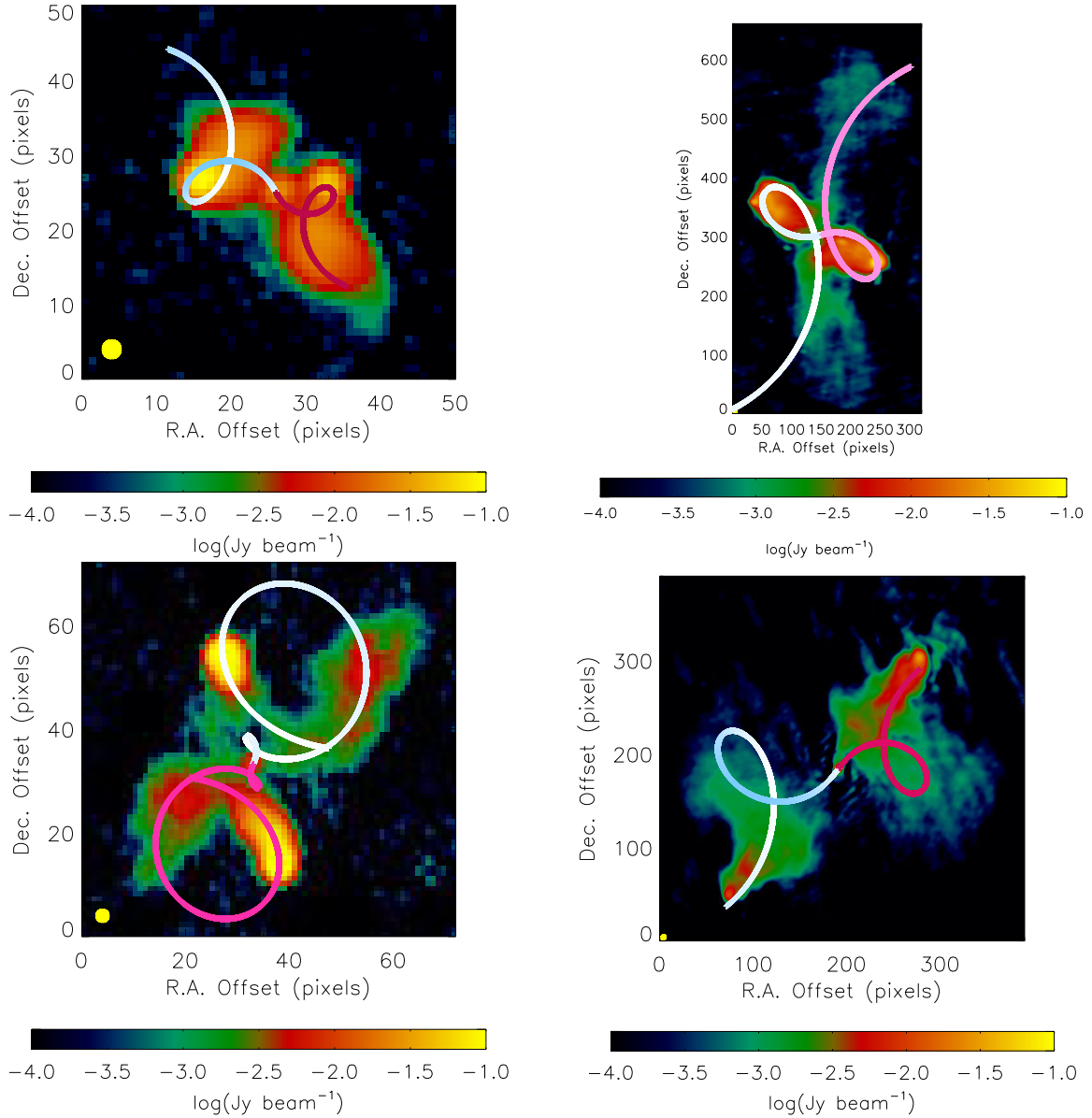


**Figure 5.** Superposition of the jet and counter-jet precession helices (blue and purple hues, respectively) generated from the parameters listed in Table 4 on the kiloparsec-scale images of J1430 + 5217 (1.4 GHz, 1 pixel = 1.8 arcsec, upper left panel), 4C + 32.25 (0.4 GHz, 1 pixel = 1.3104 arcsec, upper right panel), 3C 223.1 (1.4 GHz, 1 pixel = 1.8 arcsec, lower left panel), and 4C + 61.23 (1.25 GHz, 1 pixel = 0.5796 arcsec, lower right panel) Lighter colours used in the precession helices represent higher Doppler boosting factors. The solid ellipse in the lower left corner of the individual panels represents the FWHM of the elliptical synthesized CLEAN beam.

where  $\Delta t_{\text{obs}} = t_{\text{obs}} - t_{\text{ej}}$  and the signs ‘+’ and ‘-’ refer respectively to the jet and counter-jet.

The variables  $\mu$  and  $\eta$  are calculated from equations (8)–(15) in Caproni, Monteiro & Abraham (2009), while  $\Delta t_{\text{obs}}$  is derived from equations (16)<sup>4</sup> and (17) in Caproni, Monteiro & Abraham (2009) as well. More details concerning the jet precession model for each radio galaxy are provided below, including the acceptable ranges for each individual jet precession parameter (estimated from visual inspection after varying one of the free model parameters, keeping the remaining ones fixed).

<sup>4</sup>The sign ‘-’ in this equation (Doppler boosting factor) must be replaced by the sign ‘+’ for the counter-jet.

#### 4.5.1 J1430 + 5217

The upper left panel of Fig. 5 shows the brightness distribution at 1.4 GHz of the quasar J1430 + 5217. The brighter regions were labeled as east (E) and west (W) lobes, while more diffuse and extended regions were labeled as north (N) and south (S) wings (Lal et al. 2019). Moreover, the northeast (NE) jet of J1430 + 5217 is shorter in length than the southwest (SW) jet, even though the former is brighter, in contradiction with the usual behavior of the jet being more extended and brighter than the counter-jet. Precession helices generated from the set of parameters listed in Table 4 are superposed on the 1.4 GHz map of J1430 + 5217, with the jet pointing towards the NE-direction. This precession model recovers quite well the position of the E and W lobes, as well as the nowadays

position angle of its parsec-scale jet seen in Fig. 4 ( $\sim 30^\circ$ , measured from N to E direction). Doppler boosting factor for the jet (counter-jet) ranges from 1.198 to 1.282 (0.778–0.813). Even though our non-accelerating precession model overestimates the total length of the jet at 1.4 GHz, any deceleration of the jet material due to its propagation in a denser environment could bring the tip of the jet helix closer to the N wing.

Acceptable precession models are found for  $4.0 \leq P_{\text{prec, obs}}(\text{Myr}) \leq 10.0$ . Periods shorter than 4.0 Myr put the precession loop seen in Fig. 5 between the core and W lobe, besides decreasing substantially the precession amplitude. On the other hand, precession periods longer than 10 Myr lead to a loop's position farther than the W lobe. For the remaining model parameters, we obtained the ranges  $0.125 \leq \beta \leq 0.312$ ,  $20^\circ \leq \phi_0 \leq 32^\circ$ ,  $8^\circ \leq \varphi_0 \leq 20^\circ$ ,  $54^\circ \leq \eta_0 \leq 85^\circ$ .

#### 4.5.2 4C + 32.25

The complex radio structure observed at kiloparsec-scale radio images of 4C + 32.25 are essentially formed by brighter east and west radio lobes with hotspots at their ends and fainter and more extended north and west wings (e.g. Parma, Ekers & Fanti 1985). We modeled these radio structures in terms of a precessing jet with a constant speed of  $0.033c$  and a period of about 87.5 Myr. The remaining precession parameters are given in Table 4, while the precession helices associated with it are shown in Fig. 5. Although this precession model assumes that the east lobe and the south wing belong to the jet, another scenario where the jet would be related to the west lobe and the north wing is also possible. Acceptable precession models can also be found for the ranges  $40 \leq P_{\text{prec, obs}}(\text{Myr}) \leq 500$ , even though  $P_{\text{prec, obs}} > 90$  Myr would imply an age for the wings older than about 70 Myr, age estimated by Klein et al. (1995),  $0.006 \leq \beta \leq 0.072$ ,  $25^\circ \leq \phi_0 \leq 51^\circ$ ,  $23^\circ \leq \varphi_0 \leq 49^\circ$ ,  $90^\circ \leq \eta_0 \leq 120^\circ$ .

Jet precession in 4C + 32.25 was already invoked in previous works (Parma, Ekers & Fanti 1985; Klein et al. 1995), even though qualitatively. For instance, Klein et al. (1995) proposed a precession period of 200 Myr, while Parma, Ekers & Fanti (1985) suggested the values of  $25^\circ$  and  $60^\circ$  for the precession angle and the viewing angle of the precession cone axis. These values are compatible with those estimated in this work.

#### 4.5.3 3C 223.1

The X-shaped source 3C 223.1 shows two pairs of structures at kiloparsec-scales: lower brightness surface lobes (labeled as East and West wings in Lal & Rao 2005) with flatter spectral indices in comparison with the higher brightness surface lobes (labeled as North and South lobes in Lal & Rao 2005). It implies that North and South lobes are more aged structures than East and West wings (Dennett-Thorpe et al. 2002; Lal & Rao 2005, 2007), imposing an important constraint for the jet precession modeling. Indeed, the precession model for 3C 223.1 shown in Fig. 5 respects these findings since the jet (counter-jet) helix crosses the North (South) lobe firstly, reaching the West (East) wing after  $\sim 3$  Myr for this particular set of parameters. This precession model also predicts the correct orientation of the parsec-scale jet of 3C 223.1 at 5 GHz (position angle  $\sim -25^\circ$ ; see Fig. 4). Doppler boosting factor for the jet (counter-jet) ranges from 1.075 to 1.094 (from 0.914 to 0.928). Acceptable precession models can also be found for the ranges  $1.5 \leq P_{\text{prec, obs}}(\text{Myr}) \leq 20.9$ ,  $0.035 \leq \beta \leq 0.46$ ,  $15^\circ \leq \phi_0 \leq 42^\circ$ ,  $10^\circ \leq \varphi_0 \leq 35^\circ$ ,  $310^\circ \leq \eta_0 \leq 15^\circ$ . Gong, Li & Zhang (2011) also modeled this source in terms of jet precession, determining a precession period of

$\sim 1.8$  Myr,  $\phi_0 \sim 36^\circ$  and  $\varphi_0 \sim 26^\circ$ , all of them in the parameters' ranges estimated in this work.

Furthermore, no radio emission is seen between the North lobe and the West wing, as well as between the South lobe and the East wing. It might indicate an intermittent AGN activity in 3C 223.1 that, in terms of the precession model shown in Fig. 5, would represent a substantial decrease of the jet activity during about 3 Myr. Surprisingly, a similar 3-Myr interruption of the jet activity might be associated with the brightness gap seen right above the core (at the location of the small jet precession loop seen in Fig. 5), even though the south counterpart of this gap is not observed at 1.4 GHz.

#### 4.5.4 4C + 61.23

This radio galaxy exhibits two hotspots at the end of its pair of kiloparsec-scale lobes, oriented along northwest–southeast (NW–SE) direction on the plane of the sky. Two additional NE–SW oriented structures are continuously connected with the radio lobes that could be formed by backflows from the lobes (Lara et al. 2001). In this work, we investigated the possibility that such complex structures could be mainly produced by precessing jets.

We show the precession helices in Fig. 5 generated by the model parameters provided in Table 4. Overall agreement between model and image can be seen in this figure, suggesting that NE–SW structures could be produced by a precessing jet. Our kiloparsec-scale precession model for 4C + 61.23 also correctly predicts the current position angle of the parsec-scale jet seen in VLBI images of this source (Liu et al. 2018). Jet is assumed to point towards SE direction, which is corroborated by the more distant location of the SE hot-spot from the core region of 4C + 61.23 in comparison with the NW hot-spot, as well as from VLBI observations of this source, for which its parsec-scale jet seems to be pointing to southeast (Liu et al. 2018). Note that the SE lobe seems slightly fainter than the NW lobe, contrary to what would be expected in this case, indicating some hydrodynamic effects on the jet propagation that are not considered in our pure kinematic precession model.

Fair precession models can be found for the following parameter ranges:  $4.5 \leq P_{\text{prec, obs}}(\text{Myr}) \leq 70.0$ ,  $0.018 \leq \beta \leq 0.279$ ,  $25^\circ \leq \phi_0 \leq 35^\circ$ ,  $12^\circ \leq \varphi_0 \leq 22^\circ$ ,  $100^\circ \leq \eta_0 \leq 111^\circ$ .

#### 4.5.5 B2 1059 + 29

This radio galaxy shows an S-symmetry morphology at the Band 5 map, with the SW lobe brighter than the NE one. It suggests its jet is pointing toward the SW direction. However, the NE structure is more extended than the SW lobe, which contradicts the former possibility. Unfortunately, no parsec-scale image of B2 1059 + 29 that could shed some light on this contradictory finding is available in the literature, obligating us to consider both possibilities in this work.

We show in Fig. 6 two viable jet precession models, one associating the NE lobe with the kiloparsec-scale jet of B2 1059+29 (left panel) and the other with the jet oriented southwestward (right panel). Besides the jet orientation, these two models differ mainly in terms of the precession period, having the SW model a precession period twice longer than that assumed in the NE precession model. Even though the NE jet precession model seems to be slightly better in comparison with the SW model due to the NE precession helix fully covers the total extension of the NE lobe of B2 1059 + 29, a roughly W-oriented motion of the galaxy might boost the brightness of the SW lobe, as well as increase (decrease) the length of the NE (SW)

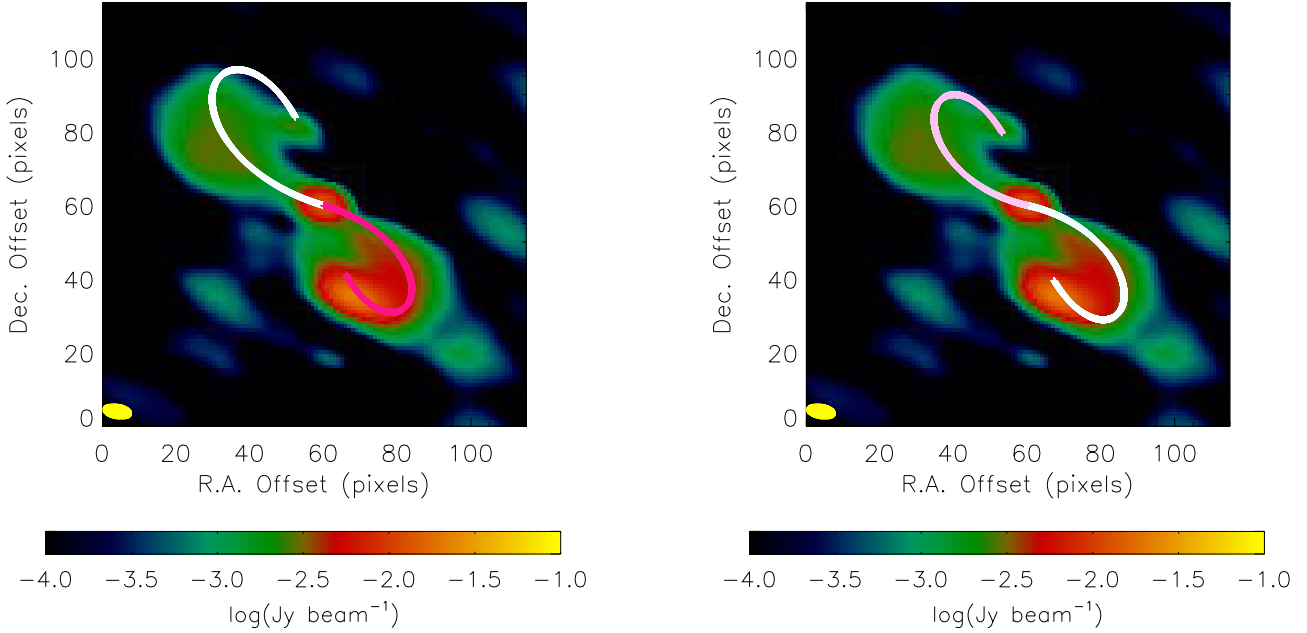


**Figure 6.** Superposition of the jet and counter-jet precession helices (blue and purple hues, respectively) generated from the parameters listed in Table 4 on the kiloparsec-scale image of B2 1059 + 29 (1.25 GHz, 1 pixel = 0.5508 arcsec). Given the contradictory findings regarding surface brightness and total length of the pair of lobes, we have considered two distinct scenarios where that jet points towards the NE direction (left panel) and the SW direction (right panel). Lighter colours used in the precession helices represent higher Doppler boosting factors. The ellipse in the lower left corner of the individual panels represents the FWHM of the elliptical synthesized CLEAN beam.

lobe. In this case, the SW model could be preferable. This possibility will be analysed in more detail using hydrodynamic simulations in future work.

Precession model parameters that produce fair agreements with the radio structures of B2 1059 + 29 are  $25.0 \leq P_{\text{prec, obs}} (\text{Myr}) \leq 140.0$ ,  $0.041 \leq \beta \leq 0.230$ ,  $5.8^\circ \leq \phi_0 \leq 21^\circ$ ,  $5.7^\circ \leq \varphi_0 \leq 20.9^\circ$ ,  $85^\circ \leq \eta_0 \leq 105^\circ$  in the case of NE-oriented jet. In contrast, the ranges  $40.0 \leq P_{\text{prec, obs}} (\text{Myr}) \leq 180.0$ ,  $0.008 \leq \beta \leq 0.037$ ,  $10.0^\circ \leq \phi_0 \leq 41^\circ$ ,  $9.9^\circ \leq \varphi_0 \leq 40.9^\circ$ ,  $269^\circ \leq \eta_0 \leq 285^\circ$  are applicable for the case of a jet oriented southwestward.

## 5 DISCUSSION

In this section, we explore the three different signatures that point to the presence of BBH and the feasibility of a BBH model. We will discuss each signature independently and then consider how they compare with each other for a comprehensive understanding.

### 5.1 Role of BBH in double-peaked emission lines

Assuming that the double-peaked [O III] emission line has its origin from the BBHs, it is possible to calculate the separation between the black holes,  $d_{\text{BH}}$ , through

$$d_{\text{BH}} = \frac{GM_{\text{tot}}}{\Delta v^2}, \quad (9)$$

where  $G$  is the gravitational constant and  $\Delta v$  is the velocity separation of the blueshift and redshift line components.

Using the values of  $M_{\text{tot}}$  given in Table 3, as well as the measured velocity separation between the [O III] emission lines, we obtain for  $d_{\text{BH}} = 11.8 \pm 4.6$  pc for J1430+5217,  $8.9 \pm 1.7$  pc for 4C+32.25,  $7.1 \pm 1.5$  pc for 3C 223.1,  $6.4 \pm 1.8$  pc for 4C+61.23, and  $4.5 \pm 0.9$  pc for B2 1059 + 29.

**Table 5.** NLR region sizes for the DP emission lines.

Source name	NLR size of blueshifted component (kpc)	NLR size of redshifted component (kpc)
4C32.25	$(1.54 \pm 0.17)$	$(1.65 \pm 0.18)$
3C223.1	$(3.69 \pm 0.26)$	$(4.13 \pm 0.28)$
B21059 + 29	$(2.88 \pm 0.23)$	$(2.70 \pm 0.22)$
4C61.23	$(5.6 \pm 0.4)$	$(4.76 \pm 0.31)$
J1430 + 5217	$(5.9 \pm 0.4)$	$(5.31 \pm 0.34)$

The size of the NLR can be obtained using the relation derived in Liu et al. (2013),

$$\log \left( \frac{R_{\text{NLRs}}}{\text{pc}} \right) = (0.250 \pm 0.018) \times \log \left( \frac{L_{[\text{OIII}]}}{10^{42} \text{ erg s}^{-1}} \right) + (3.746 \pm 0.028) \quad (10)$$

We estimate the size of the NLR region for all our sources using the above equation. The [O III] luminosities are taken from Ge et al. (2012). The sizes of the NLR regions for both the redshifted and blueshifted components were computed separately and are provided in Table 5.

To explain the BBH model successfully, the size of the NLR regions ideally should not be greater than BH separations. However, we derive black hole separation much smaller than the estimated NLR sizes in all our sample galaxies. Such a significant disparity in the size scales argues against a scenario where BBHs could be the primary cause of the double-peaked emission lines. However, it has to be noted that these are merger systems, and the standard empirical relation need not apply in this case. Moreover, while the NLR could extend to sizes as large as a few kpcs, the NLR emission may be more concentrated in the inner pc-scale regions, which are influenced by the individual black holes, possibly leading to the double-peaked emission lines. We cannot spatially resolve the

NLR with optical spectroscopy, so the exact nature or the extent of NLR remains uncertain. There may be a complex structure in the NLR (Popović 2012); for instance, the NLR may have been tidally disrupted, leaving only a small core component around each BH (Haas et al. 2005; Baum et al. 2010). It is interesting to note that the double-peak is present not only in [O III] emission lines but also in the H  $\beta$  (BLR) regions (see Fig. 1 for example). Hence, at this point, it is impossible to rule out the BBH scenario completely.

Another likely explanation for the double-peaked emission lines in the spectra is the jet-driven outflows. Given that all our sample galaxies have jets that extend over a few kpc, it is possible that the gas in the NLR is being pushed away, leading to the double peak seen in the optical spectra (Stockton et al. 2007; Kharb et al. 2017b, 2019). The outflow velocities in a jet-driven outflow could also range from 50 to several 100s of km s<sup>-1</sup> (see for example, Mahony et al. 2016). Hence, it is hard to distinguish between the two possible mechanisms that give rise to the double peak.

Another possible explanation for the origin of the double-peak is peculiar disc kinematics. Owing to the high AGN-related [O III] luminosity, which is unlikely to be distributed in a disc. NLR-related [O III] emission is often distributed in biconical structures (Falcke, Wilson & Simpson 1998) rather than a rotating disc. Moreover, the optical hosts of radio-loud sources are early-type galaxies like ellipticals, often lacking a well-defined disc (Best et al. 2005).

Future observations characterizing the spatial distribution of the [O III] emission, either using narrow-band imaging or IFS, can help distinguish between the various models.

## 5.2 Precession and the role of BBH

The interaction of BBHs can give rise to inverse symmetric radio jet geometries like X, S, and Z shapes. The peculiar morphology could be either due to jet reorientation or jet precession in the presence of a companion galaxy. There are arguments in the literature suggesting that X or S-shaped morphology can also be due to the back-flow of gas. There are, however, confirmed DAGN (NGC 326) or binary systems (SS433 microquasar) whose morphologies are well explained by jet precession. Hjellming & Johnston (1981) proposed a kinetic model to explain the radio jets from X-ray binary SS433 without assuming the origin of jet precession.

Nandi et al. (2021) analysed three distinct jet precession scenarios in the case of the radio galaxy J1328 + 2752: misaligned accretion disc with the orbital plane of the BBHs (e.g. Sillanpaa et al. 1988; Katz 1997; Caproni et al. 2017), geodetic precession (e.g. Barker & O’Connell 1975; Krause et al. 2019), both scenarios involving supermassive BBHs, and the Bardeen–Peterson effect (BP; e.g. Bardeen & Peterson 1975; Caproni, Abraham & Mosquera Cuesta 2006a; Caproni et al. 2006b; Martin, Pringle & Tout 2007), where precession is induced by a single (spinning) black hole. Here, we will follow Nandi et al. (2021), analysing the feasibility of these scenarios for the remaining five radio galaxies of our sample that present double-peaked emission lines besides signatures of jet precession.

### 5.2.1 Geodetic precession

The black hole separations derived in Section 5.1 imply orbital periods at the observer’s reference frame,  $P_{\text{orb, obs}}$ ,<sup>5</sup> equals to 206 ± 128 kyr, 171 ± 51 kyr, 152 ± 51 kyr, 131 ± 57 kyr, and 66 ± 22 kyr, for

J1430+5217, 4C+32.25, 3C 223.1, 4C+61.23 and B2 1059 + 29 respectively.

In the case of the geodetic precession, the minimum value of the precession period,  $P_{\text{prec}}^{\text{geo, min}}$  is

$$\left( \frac{P_{\text{prec}}^{\text{geo, min}}}{\text{Gyr}} \right) \cong 0.071 \left( \frac{d_{\text{BH}}}{1\text{pc}} \right)^{5/2} \left( \frac{M_{\text{tot}}}{10^9 M_{\odot}} \right)^{-3/2} \quad (11)$$

which was obtained after assuming  $q_{\text{BH}} = M_{\text{BH, s}}/M_{\text{BH, p}} = 1$  in the original equation provided, e.g. by Krause et al. (2019), where  $M_{\text{BH, p}}$  and  $M_{\text{BH, s}}$  are respectively the mass of the primary (the driver of the jet) and secondary SMBHs in a binary system. Using equation (11), we found  $P_{\text{prec}}^{\text{geo, min}} = 171 \pm 166$  Gyr for J1430+5217,  $174 \pm 92$  Gyr for 4C+32.25,  $191 \pm 117$  Gyr for 3C 223.1,  $149 \pm 120$  Gyr for 4C+61.23, and  $39 \pm 24$  Gyr for B2 1059 + 29, values incompatible with the precession periods estimated in Section 4.5 for these sources. Moreover, these are much higher than the age of the Universe, further invalidating them. It implies that geodetic precession cannot be the mechanism behind the jet precession inferred from our kinematic models.

### 5.2.2 Misaligned accretion disc

Another possibility in the framework of binary systems is the precession induced by a secondary black hole in a non-coplanar orbit around the primary one. If the outer radius of the primary accretion disc is  $R_{\text{out, p}}$ , the precession period can be estimated as (e.g. Nandi et al. 2021)

$$[K(s) \cos \varphi_0] \left( \frac{P_{\text{prec, obs}}}{P_{\text{orb, obs}}} \right) = \left[ \frac{(1 + q_{\text{BH}})^{1/2}}{q_{\text{BH}}} \right] \left( \frac{R_{\text{out, p}}}{d_{\text{BH}}} \right)^{-3/2}, \quad (12)$$

where  $K(s) \approx 0.19 - 0.47$  for a power-law surface density accretion disc with an index  $s$  between 0 and -2 (Larwood et al. 1996; Bate 2000).

We show in Fig. 7 the precession period at the observer’s reference frame times the cosine of the precession angle as a function of  $q_{\text{BH}}$ . Solutions represented by blue stripes were obtained assuming  $R_{\text{out, p}}$  equals the tidal radius of the BBH (e.g. Papaloizou & Pringle 1977; Romero et al. 2000; Caproni et al. 2017), while those found from a fixed value of  $R_{\text{out, p}}$  (0.01, 0.1 and 1.0 pc, typical values for which AGN accretion discs become gravitationally unstable; e.g. Goodman 2003; King & Pringle 2007) are displayed by hatched red stripes. In addition, yellow stripes show the ranges for  $\cos \varphi_0 P_{\text{prec, obs}}$  derived in Section 4.5. Precession induced by a non-coplanar secondary is possible only if  $q_{\text{BH}} \gtrsim 0.012$  for 4C + 32.25, while  $q_{\text{BH}} \gtrsim 0.029$  is applicable for 4C+61.23. For J1430 + 5217 and 3C 223.1, the lower limits for  $q_{\text{BH}}$  are respectively 0.18 and 0.13. As the precession modeling for B2 1059 + 29 led to two distinct scenarios for its jet precession, we analysed both possibilities in the context of the present physical mechanism, resulting in the bottom panels in Fig. 7. In the case of a jet oriented northeastward,  $q_{\text{BH}} \gtrsim 0.005$  makes this precession mechanism compatible with our jet precession modeling, similar to the results obtained for the jet pointing SW,  $q_{\text{BH}} \gtrsim 0.004$ . Therefore, jet precession induced by torques in the primary accretion disc due to a secondary black hole with an orbit non-coplanar with the primary black hole is a viable mechanism for 4C+32.25, 4C+61.23, and B2 1059 + 29.

### 5.2.3 BP

Finally, disc precession can be driven by the combination of the accretion disc’s viscosity and the Lense–Thirring effect (Lense &

<sup>5</sup>Calculated using Kepler’s third law, i.e.  $P_{\text{orb, obs}} = 2\pi a_{\text{BH}}^{3/2} / \sqrt{GM_{\text{tot}}}$ .

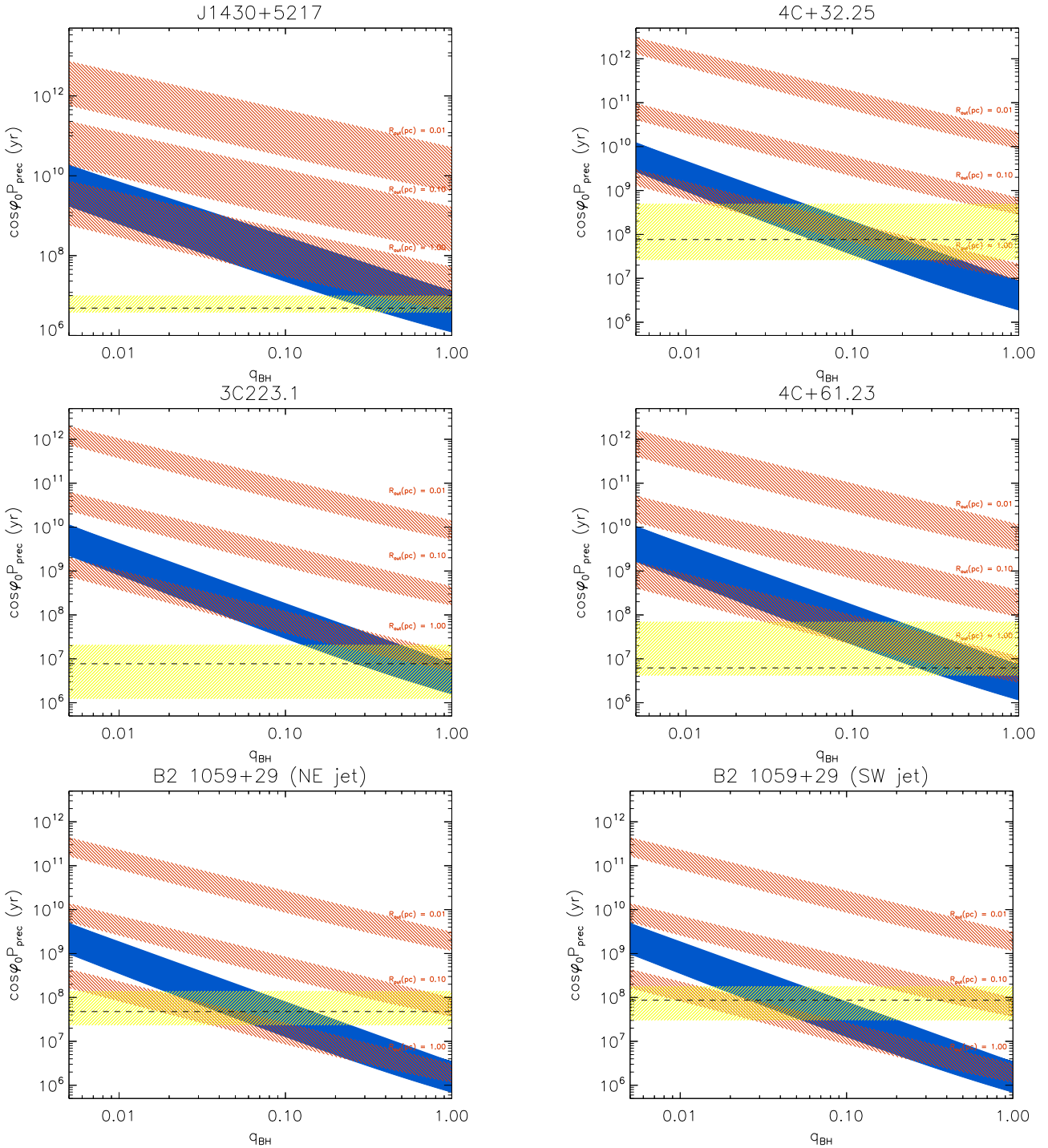


**Figure 7.** Behaviour of  $\cos \varphi_0 P_{\text{prec, obs}}$  as a function of  $q_{\text{BH}}$  due to precession of the primary’s accretion disc induced by a secondary black hole in a non-coplanar orbit around the primary one. Slanted solid stripes refer to  $\cos \varphi_0 P_{\text{prec, obs}}$  at  $1\sigma$ -level calculated from equation (6) in Nandi et al. (2021) assuming that the outer radius of the disc is the tidal radius. Slanted hatched stripes use the same equation but with the outer radius of the disc set as the values 0.01, 0.1, and 1 pc. Hatched horizontal rectangles represent the lower and upper conservative limits for  $\cos \varphi_0 P_{\text{prec, obs}}$  expected for each source. The dashed horizontal line refers to the jet precession model listed in Table 4.

Thirring 1918) due to the misalignment between the angular momenta of the disc and of a Kerr black hole, a mechanism known in the literature as BP (Bardeen & Petterson 1975). We analysed the feasibility of the BP effect to be responsible for precession in the sources 4C+32.25, 4C+61.23, and 3C223.1 only since no

information regarding the bolometric luminosity of B2 1059+29, and J1430+5217 were found in the literature. We follow strictly the formalism adopted in Nandi et al. (2021; section 3.3 in their paper), assuming  $\alpha = 0.1$ , the standard viscosity parameter introduced by Shakura & Sunyaev (1973), and an outer radius for the accretion

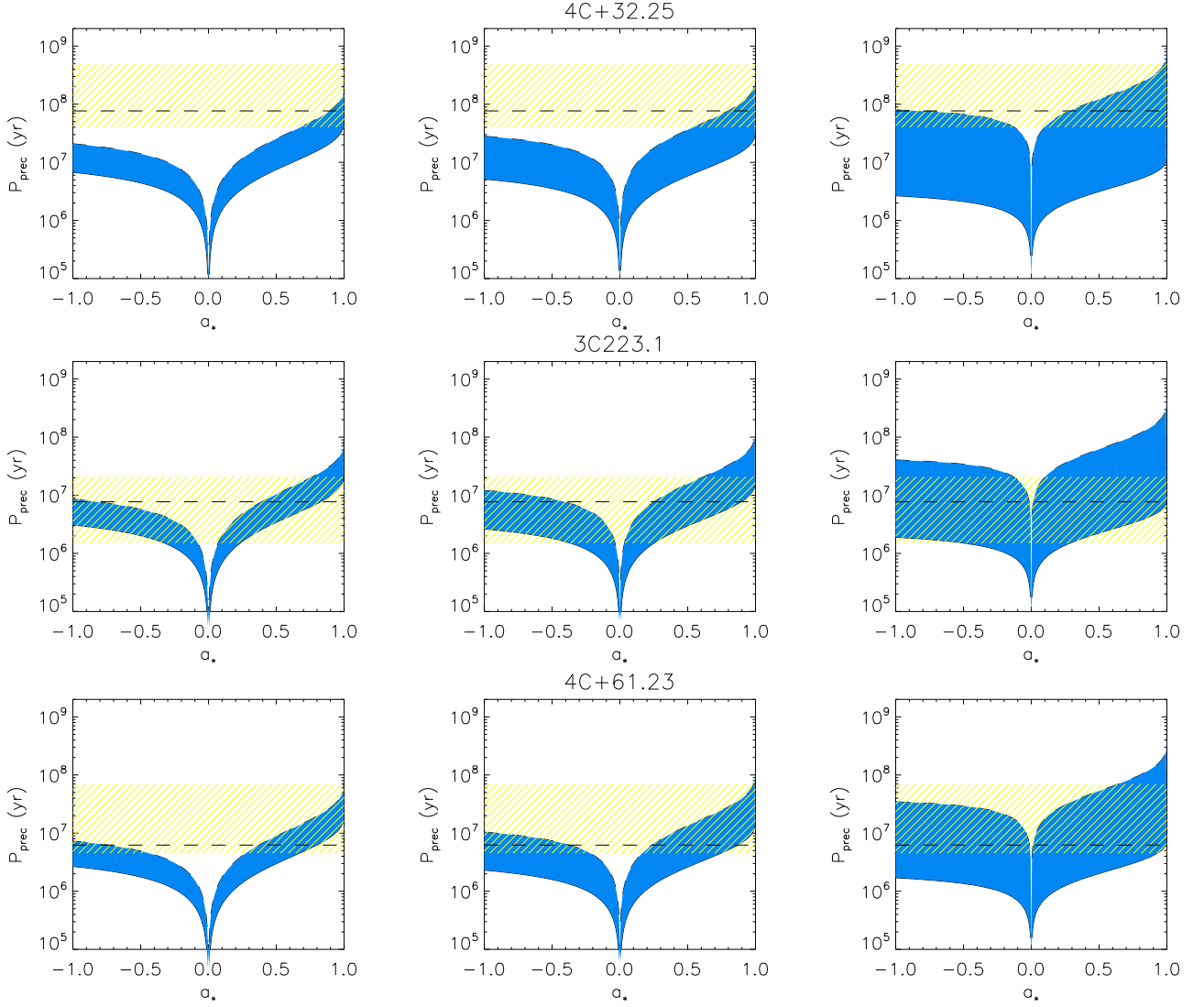


**Figure 8.** Precession period induced by the BP effect as a function of  $a_*$  for 4C+32.25, 3C 223.1 and 4C + 61.23 (top to bottom panels, respectively). It was assumed in the calculations  $\alpha = 0.1$  and  $R_{\text{out},p} = 0.05$  parsec. Solutions for  $s = -2, -1$ , and  $0$  are shown from left to right. Upper and lower envelopes of the solid stripes for  $P_{\text{prec,BP}}$  refer respectively to the lower and upper values of  $\Sigma_0$ . The hatched rectangle delineates the lower and upper conservative limits for  $P_{\text{prec,obs}}$  expected for each source.

disc of 0.05 parsec. We have made use of the same notation as in Nandi et al. (2021). The bolometric luminosity,  $L_{\text{bol}}$ , for 4C+32.25, 3C 223.1 and 4C + 61.23 are, respectively,  $8.13 \times 10^{44}$ ,  $1.15 \times 10^{45}$ , and  $1.34 \times 10^{45}$  erg s $^{-1}$  (Trichas et al. 2013; Kong & Ho 2018), which turns out to be respectively  $l = L_{\text{bol}}/L_{\text{Edd}} = 0.026, 0.058$ , and  $0.068$  after estimating the Eddington luminosity,  $L_{\text{Edd}}$ , from  $M_{\text{tot}}$  given in Table 3. The results are shown in Fig. 8, considering three different power-law indices,  $s$ , for the surface density of their accretion discs.

We can note that the BP effect induces precession time-scales compatible with the estimated range for the jet precession period in 4C + 61.23 for the three values of  $s$  ( $-2, -1$ , and  $0$ ), even though not for all values of  $a_*$ , a dimensionless parameter corresponding to the ratio between the actual angular momentum of the black hole and its maximum possible value. Indeed, only  $a_*$  lower than about  $-0.6$  (antiparallel angular momentum vectors of the disc and the black hole) or higher than  $0.3$  (parallel angular momentum vectors of the

disc and the black hole) produces precession time-scales compatible with those inferred from the radio maps for  $s = -2$ . At the same time, less restrictive ranges for  $a_*$  are found for  $s = -1$  and  $0$  (e.g. BP effect is ruled out for  $-0.2 < a_* < 0.2$  in the case of  $s = -1$ ). Similar behavior was found for 3C 223.1, but with almost all values of  $a_*$  and  $s$  allowed for this source. For the source 4C + 32.25, the BP effect is only feasible for prograde rotation with  $a_* \gtrsim 0.5$  in the case of  $s = -2$  and  $s = -1$ . For a constant surface density profile ( $s = 0$ ), retrograde rotation is marginally possible only if  $a_* \lesssim -0.2$ . Therefore, the BP mechanism cannot be ruled out as a potential precession driver in the case of the sources 4C+32.25, 3C 223.1, and 4C + 61.23.

### 5.3 Dual VLBA compact components and the role of BBH

From our sample of six X-shaped radio galaxies with double-peaked narrow emission lines in optical spectra, we detect double VLBA

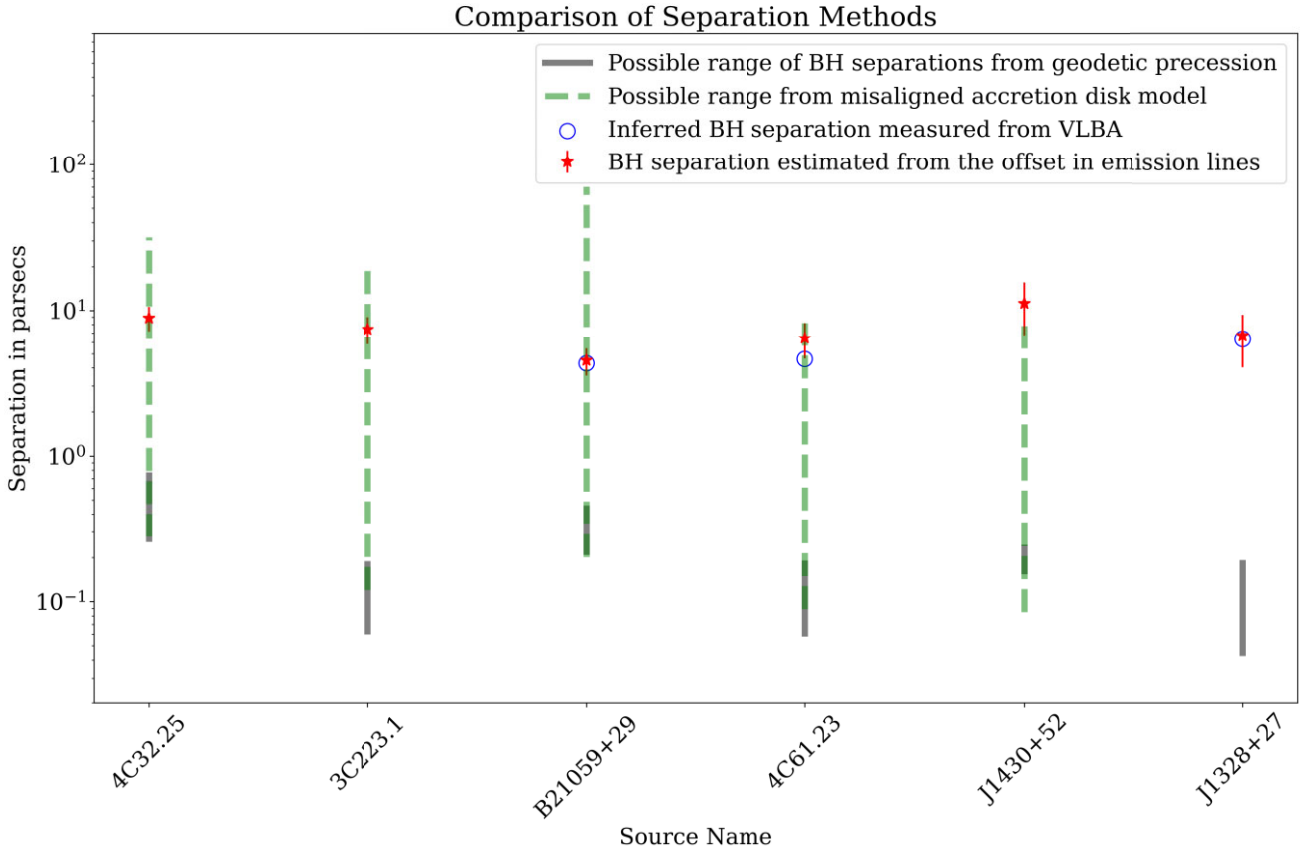


**Figure 9.** Comparison of black hole separation methods. The plot illustrates the possible range of black hole separations from geodetic precession, misaligned accretion disc models estimated separation from the offset in emission lines, and inferred separation measured from VLBA. The separations derived from geodetic precession are inconsistent with those derived from the offsets in the emission lines and the VLBA compact components separation. However, the range of black hole separation predicted by the misaligned accretion disc model is consistent with the separation derived from emission lines. The correlation between the expected separation derived from the emission lines offset and the VLBA components’ physical separation is significant. It is important to note that any minor differences observed between the separations estimated from both methods could also, in principle, be introduced by projection effects.

compact components in three sources. From low-resolution GMRT images, the cores of both 4C 61.23 and J1328+27 exhibit flat-spectrum, whereas B2 1059 + 29 possess a steep spectrum compact component at the centre. A steep core spectral index often indicates that extended structures dominate the emission within the unresolved beam (e.g. Marecki, Sebastian & Ishwara-Chandra 2023). Hence, the structure seen in B2 1059 + 29 might be a CSO (O’Dea & Saikia 2021).

Obtaining quasi-simultaneous multifrequency observations is crucial to discern the true nature of the components. If both VLBA components are found to possess a flat or an inverted radio spectrum, it would strongly imply that the compact components are AGN cores. One steep spectrum and one flat/inverted spectrum core would indicate a core-jet structure; finally, two steep spectrum components could suggest the presence of a CSO. Hence, the lack of separate spectral index information for both components prevents us from ruling out or confirming the BBH scenario for the double VLBA components.

#### 5.4 Comparison: feasibility of the BBH model

We have three indicators that predict the presence of BBH in three of our sample galaxies and at least two in the rest of the sample.

A more conclusive test is to compare the physical properties of the BBH derived from these three separate diagnostics. Fig. 9 shows a comparison between the BH separation predicted from the three different BBH diagnostics (see Sections 5.1, 5.2, and 4.2). The values predicted by the geodetic precession model are inconsistent with the other black hole separations and require the black holes to be closer than those predicted by the VLBA by at least one order of magnitude (see Section 4.4). Note that all the methods result in black hole separations on parsec scales.

We estimate the range of black hole separations ( $d_{\text{BH}}$ ) on parsec scales predicted by the misaligned accretion disc model for each target is obtained by inverting equation (12). Specifically, the lower boundary arises when  $s = -2$  and  $R_{\text{out},p} = 0.01$  pc, while the upper limit is for  $s = 0$  and  $R_{\text{out},p}$  equal to the tidal radius of the BBH. Although geodetic precession models disagree with the separations predicted by the other two methods, the misaligned accretion disc model can successfully explain the observed black hole separations. However, this can be partly attributed to the more significant number of free parameters in the model and uncertainties concerning our understanding of physical properties like the accretion disc radius.

On the other hand, the agreement between the predicted offset from the emission lines and the VLBA is highly encouraging. However,

we note that projection effects affect both the separation estimates, and therefore we should not expect a correlation with dispersions smaller than an order of magnitude.

Finally, we compare the occurrence rate of X-shaped sources in DPAGN with extended radio morphology with that in a general sample of extended radio sources to uncover any potential correlation between the two signatures. Suppose we recovered a higher fraction of X-/S-shaped sources from a sample of DPAGN with extended radio emission than a general sample of extended radio sources. In that case, it might suggest a common origin or, in other words, provide support for the BBH scenario. Cheung (2007, the CC07 sample) discovered  $\sim 100$  X-shaped sources from a parent sample of  $\sim 8000$  extended FIRST sources with flux densities  $> 5$  mJy through visual inspection. The original FIRST source database at the time of the publication consisted of  $\sim 800\,000$  sources. We used a similar approach, although with slight differences.

Our crossmatch of the DPAGN sample with FIRST returned  $\sim 600$  sources, out of which we found 30 extended sources and four X-shaped sources. Hence, we find that  $\sim 13$  per cent (four out of thirty) of DPAGN sources with extended radio emission show X-shaped morphology. Since Cheung (2007) does not clarify whether the sample of the X-shaped sources they identified is complete, we can only conclude that the typical fraction of cross-symmetric radio sources in a general sample of extended radio sources is  $> 1.25$  per cent. Several more cross-symmetric sources are reported in Yang et al. (2019) and Bera et al. (2020) owing to differences in classification approaches. The total number of X-/S-/Z-shaped sources among the extended sources identified from the FIRST survey is only  $\sim 400$  to date ( $\sim 5$  per cent). Hence, extended radio sources with DPAGN are at least twice as likely to possess an X-shaped radio morphology compared to a general sample of extended radio sources. This conclusion remains valid whether we start from a sample of all or merely extended radio sources. More specifically, the fraction of cross-symmetric sources identified from the entire FIRST survey catalogue (not only the extended sources) to date is  $\sim 0.04$  per cent as opposed to 0.7 per cent from a sample of FIRST sources that exhibit DPAGN.

While a higher probability for DPAGN to host more X-shaped sources argues for a BBH model in these systems, we would like to point out a few caveats. These probabilities are derived from a small sample and are prone to errors due to the small number statistics. Secondly, there might be several more X-shaped sources in the FIRST survey that remain to be discovered. Hence, while these numbers indicate the presence of underlying BBHs in many of these systems, a more rigorous statistical analysis is warranted to make more substantial claims.

Similarly, the high fraction of sources with dual radio peaks implies that our selection criterion is potentially useful in uncovering BBHs for follow-up observations.

## 6 SUMMARY AND CONCLUSIONS

We present new VLBA images at 5 and 15 GHz of six X-shaped radio galaxies with double-peaked emission lines in their optical spectra. New uGMRT images at Bands 3 and 5 (400 and 1250 MHz) of three sources are also presented. We summarize below our primary findings.

(i) Three out of six sources exhibit dual compact radio components with at least one frequency using the VLBA. These could be dual cores, core-jet components, or CSOs.

(ii) From the velocity separation of the blueshift and redshift line components detected in the optical spectra of these radio galaxies and their respective total black hole mass, we estimated the separation between the primary and secondary black holes under the hypothesis that the double lines are due to BBH in their nuclei, obtaining values roughly between 4 and 12 pc. These values are comparable to the compact component separations for the three sources with VLBA dual component detections.

(iii) The overall kpc-scale morphology of the radio galaxies in our sample is compatible with a jet/counter-jet precession scenario, even though some fine structural details in the radio images of some sources (e.g. systematic bending of the SE jet of 4C + 32.25) are not recovered by our kinematic-only jet precession model. Extra mechanisms (e.g. ram-pressure phenomenon) must act upon the kiloparsec-scale jets in these cases. Our precession models suggest that the six sources have mildly relativistic jets ( $\beta < 0.5$ ), with precession cone axes oriented between  $6^\circ$  and  $70^\circ$  to the line of sight and semi-aperture precession angles between  $3^\circ$  and  $49^\circ$ . Inferred jet precession periods on the observer's reference frame range from 1.5 to 500 Myr.

(iv) We have explored three different physical mechanisms behind jet precession: geodetic precession and precession induced by a secondary black hole in a non-coplanar orbit around the primary accretion disc, both possibilities implying the existence of a BBH system in the nuclei of our six sources, as well as the BP. Two of our six sources could not be analysed in the context of the BP due to the lack of estimates of their bolometric luminosities. While geodetic precession predicts too long precession periods compared with the estimates derived from our precession modeling, the other two scenarios provide compatible precession periods for all the sources. It supports the jet/counter-jet precession scenario for the radio galaxies of our sample, even though these analyses do not univocally favour the BBH hypothesis.

## ACKNOWLEDGEMENTS

We are grateful to the anonymous reviewer for their insightful comments, which helped improve our article. BS, CO, and SB acknowledge support from the Natural Sciences and Engineering Research Council (NSERC) of Canada. PK acknowledges the support of the Department of Atomic Energy, Government of India, under the project 12-R&D-TFR-5.02-0700. SN acknowledges support by the Science & Engineering Research Board (SERB), a statutory body of Department of Science & Technology (DST), Government of India (Scheme: State University Research Excellence (SERB SURE); File Number: SUR/2022/003864). The National Radio Astronomy Observatory is a facility of the National Science Foundation operated under a cooperative agreement by Associated Universities, Inc. Funding for the SDSS and SDSS-II has been provided by the Alfred P. Sloan Foundation, the Participating Institutions, the National Science Foundation, the U.S. Department of Energy, the National Aeronautics and Space Administration, the Japanese Monbukagakusho, the Max Planck Society, and the Higher Education Funding Council for England. The SDSS Web Site is <http://www.sdss.org/>.

## DATA AVAILABILITY STATEMENT

The data underlying this article will be shared on reasonable request to the corresponding author.



## REFERENCES

- Abazajian K. N. et al., 2009, *ApJS*, 182, 543
- Balmaverde B. et al., 2018, *A&A*, 619, A83
- Bardeen J. M., Petterson J. A., 1975, *ApJ*, 195, L65
- Barker B. M., O’Connell R. F., 1975, *ApJ*, 199, L25
- Barnes J. E., Hernquist L. E., 1991, *ApJ*, 370, L65
- Bate M. R., 2000, *MNRAS*, 314, 33
- Baum S. A. et al., 2010, *ApJ*, 710, 289
- Becker R. H., White R. L., Helfand D. J., 1995, *ApJ*, 450, 559
- Begelman M. C., Blandford R. D., Rees M. J., 1980, *Nature*, 287, 307
- Bera S., Pal S., Sasmal T. K., Mondal S., 2020, *ApJS*, 251, 9
- Best P. N., Kauffmann G., Heckman T. M., Brinchmann J., Charlot S., Ivezić Z., White S. D. M., 2005, *MNRAS*, 362, 25
- Bianchi S., Chiaberge M., Piconcelli E., Guainazzi M., Matt G., 2008, *MNRAS*, 386, 105
- Blecha L., Loeb A., Narayan R., 2013, *MNRAS*, 429, 2594
- Bon E. et al., 2012, *ApJ*, 759, 118
- Burbidge G. R., 1959, *ApJ*, 129, 849
- Caproni A., Abraham Z., 2004, *MNRAS*, 349, 1218
- Caproni A., Abraham Z., Mosquera Cuesta H. J., 2006a, *ApJ*, 638, 120
- Caproni A., Livio M., Abraham Z., Mosquera Cuesta H. J., 2006b, *ApJ*, 653, 112
- Caproni A., Monteiro H., Abraham Z., 2009, *MNRAS*, 399, 1415
- Caproni A., Abraham Z., Motter J. C., Monteiro H., 2017, *ApJ*, 851, L39
- Chen Y.-C., Hwang H.-C., Shen Y., Liu X., Zakamska N. L., Yang Q., Li J. I., 2022, *ApJ*, 925, 162
- Cheung C. C., 2007, *AJ*, 133, 2097
- Comerford J. M., Pooley D., Barrows R. S., Greene J. E., Zakamska N. L., Madejski G. M., Cooper M. C., 2015, *ApJ*, 806, 219
- Crenshaw D. M., Schmitt H. R., Kraemer S. B., Mushotzky R. F., Dunn J. P., 2010, *ApJ*, 708, 419
- Darg D. W. et al., 2010, *MNRAS*, 401, 1552
- Deane R. P. et al., 2014, *Nature*, 511, 57
- Dennett-Thorpe J., Scheuer P. A. G., Laing R. A., Bridle A. H., Pooley G. G., Reich W., 2002, *MNRAS*, 330, 609
- Doan A., Eracleous M., Runnoe J. C., Liu J., Mathes G., Flohic H. M. L. G., 2020, *MNRAS*, 491, 1104
- Ekers R. D., Fanti R., Lari C., Parma P., 1978, *Nature*, 276, 588
- Fabrika S., 2004, *Astrophys. Space Phys. Res.*, 12, 1
- Falcke H., Wilson A. S., Simpson C., 1998, *ApJ*, 502, 199
- Ferrarese L., Merritt D., 2000, *ApJ*, 539, L9
- Foreman G., Volonteri M., Dotti M., 2009, *ApJ*, 693, 1554
- Fu H., Stockton A., 2009, *ApJ*, 690, 953
- Fu H., Myers A. D., Djorgovski S. G., Yan L., 2011, *ApJ*, 733, 103
- Fu H., Yan L., Myers A. D., Stockton A., Djorgovski S. G., Aldering G., Rich J. A., 2012, *ApJ*, 745, 67
- Ge J.-Q., Hu C., Wang J.-M., Bai J.-M., Zhang S., 2012, *ApJS*, 201, 31
- Gebhardt K. et al., 2000, *ApJ*, 539, L13
- Gong B. P., Li Y. P., Zhang H. C., 2011, *ApJ*, 734, L32
- Goodman J., 2003, *MNRAS*, 339, 937
- Graham M. J. et al., 2015, *Nature*, 518, 74
- Haas M., Siebenmorgen R., Schulz B., Krügel E., Chini R., 2005, *A&A*, 442, L39
- Hennawi J. F. et al., 2006, *ApJ*, 651, 61
- Hjellming R. M., Johnston K. J., 1981, *ApJ*, 246, L141
- Hopkins P. F., 2008, PhD thesis, Harvard University, Massachusetts
- Hopkins P. F., Hernquist L., Cox T. J., Di Matteo T., Martini P., Robertson B., Springel V., 2005, *ApJ*, 630, 705
- Hudson D. S., Reiprich T. H., Clarke T. E., Sarazin C. L., 2006, *A&A*, 453, 433
- Husemann B., Heidt J., De Rosa A., Vignali C., Bianchi S., Bogdanović T., Komossa S., Paragi Z., 2020, *A&A*, 639, A117
- Intema H. T., Jagannathan P., Mooley K. P., Frail D. A., 2017, *A&A*, 598, A78
- Kale R., Shende K. M., Parekh V., 2019, *MNRAS*, 486, L80
- Katz J. I., 1997, *ApJ*, 478, 527
- Kharb P., Lal D. V., Merritt D., 2017a, *Nat. Astron.*, 1, 727
- Kharb P., Subramanian S., Vaddi S., Das M., Paragi Z., 2017b, *ApJ*, 846, 12
- Kharb P., Vaddi S., Sebastian B., Subramanian S., Das M., Paragi Z., 2019, *ApJ*, 871, 249
- Kharb P., Lena D., Paragi Z., Subramanian S., Vaddi S., Das M., Khatun R., 2020, *ApJ*, 890, 40
- Kharb P., Subramanian S., Das M., Vaddi S., Paragi Z., 2021, *ApJ*, 919, 108
- King A. R., Pringle J. E., 2007, *MNRAS*, 377, L25
- Klein U., Mack K. H., Gregorini L., Parma P., 1995, *A&A*, 303, 427
- Kocevski D. D. et al., 2015, *ApJ*, 814, 104
- Komossa S., Burwitz V., Hasinger G., Predehl P., Kaastra J. S., Ikebe Y., 2003, *ApJ*, 582, L15
- Kong M., Ho L. C., 2018, *ApJ*, 859, 116
- Krause M. G. H. et al., 2019, *MNRAS*, 482, 240
- Lal D. V., Rao A. P., 2005, *MNRAS*, 356, 232
- Lal D. V., Rao A. P., 2007, *MNRAS*, 374, 1085
- Lal D. V., Sebastian B., Cheung C. C., Pramesh Rao A., 2019, *AJ*, 157, 195
- Lara L., Cotton W. D., Feretti L., Giovannini G., Marcaide J. M., Márquez I., Venturi T., 2001, *A&A*, 370, 409
- Larwood J. D., Nelson R. P., Papaloizou J. C. B., Terquem C., 1996, *MNRAS*, 282, 597
- Leahy J. P., Williams A. G., 1984, *MNRAS*, 210, 929
- Lense J., Thirring H., 1918, *Physikalische Zeitschrift*, 19, 156
- Liu F. K., 2004, *MNRAS*, 347, 1357
- Liu X., Shen Y., Strauss M. A., Greene J. E., 2010, *ApJ*, 708, 427
- Liu X., Civano F., Shen Y., Green P., Greene J. E., Strauss M. A., 2013, *ApJ*, 762, 110
- Liu X., Lazio T. J. W., Shen Y., Strauss M. A., 2018, *ApJ*, 854, 169
- Lotz J. M., Jonsson P., Cox T. J., Primack J. R., 2010, *MNRAS*, 404, 575
- Mahony E. K., Oonk J. B. R., Morganti R., Tadhunter C., Bessiere P., Short P., Emonts B. H. C., Oosterloo T. A., 2016, *MNRAS*, 455, 2453
- Marecki A., Sebastian B., Ishwara-Chandra C. H., 2023, *MNRAS*, 518, L83
- Martin R. G., Pringle J. E., Tout C. A., 2007, *MNRAS*, 381, 1617
- Maschmann D., Halle A., Melchior A.-L., Combes F., Chilingarian I. V., 2023, *A&A*, 670, A46
- Merritt D., Ekers R. D., 2002, *Science*, 297, 1310
- Müller-Sánchez F., Comerford J. M., Nevin R., Barrows R. S., Cooper M. C., Greene J. E., 2015, *ApJ*, 813, 103
- Myers A. D., Brunner R. J., Nichol R. C., Richards G. T., Schneider D. P., Bahcall N. A., 2007, *ApJ*, 658, 85
- Nandi S., Jamroz M., Roy R., Larsson J., Saikia D. J., Baes M., Singh M., 2017, *MNRAS*, 467, L56
- Nandi S., Caproni A., Kharb P., Sebastian B., Roy R., 2021, *ApJ*, 908, 178
- Nelson C. H., 2000, *ApJ*, 544, L91
- O’Dea C. P., Owen F. N., 1987, *ApJ*, 316, 95
- O’Dea C. P., Saikia D. J., 2021, *A&A Rev.*, 29, 3
- O’Neill S. et al., 2022, *ApJ*, 926, L35
- Pacholczyk A. G., 1970, *Radio Astrophysics. Nonthermal Processes in Galactic and Extragalactic Sources.* W. H. Freeman and Company, San Francisco
- Papaloizou J., Pringle J. E., 1977, *MNRAS*, 181, 441
- Parma P., Ekers R. D., Fanti R., 1985, *A&AS*, 59, 511
- Pihajoki P., 2016, *MNRAS*, 457, 1145
- Popović L. Č., 2012, *New A Rev.*, 56, 74
- Rau U., Cornwell T. J., 2011, *A&A*, 532, A71
- Rees M. J., 1978, *Nature*, 275, 516
- Rodríguez C., Taylor G. B., Zavala R. T., Peck A. B., Pollack L. K., Romani R. W., 2006, *ApJ*, 646, 49
- Romero G. E., Chajet L., Abraham Z., Fan J. H., 2000, *A&A*, 360, 57
- Rosario D. J., Shields G. A., Taylor G. B., Salviander S., Smith K. L., 2010, *ApJ*, 716, 131
- Rottmann H., 2001, PhD thesis
- Rubinur K., Das M., Kharb P., Honey M., 2017, *MNRAS*, 465, 4772
- Rubinur K., Das M., Kharb P., 2019, *MNRAS*, 484, 4933
- Sexton R. O., Matzko W., Darden N., Canalizo G., Gorjian V., 2021, *MNRAS*, 500, 2871
- Shakura N. I., Sunyaev R. A., 1973, *A&A*, 24, 337
- Shen Y., Liu X., Greene J. E., Strauss M. A., 2011, *ApJ*, 735, 48

- Sillanpaa A., Haarala S., Valtonen M. J., Sundelius B., Byrd G. G., 1988, *ApJ*, 325, 628
- Smith K. L., Shields G. A., Bonning E. W., McMullen C. C., Rosario D. J., Salviander S., 2010, *ApJ*, 716, 866
- Stockton A., Canalizo G., Fu H., Keel W., 2007, *ApJ*, 659, 195
- Tingay S. J., Wayth R. B., 2011, *AJ*, 141, 174
- Tremaine S. et al., 2002, *ApJ*, 574, 740
- Trichas M. et al., 2013, *ApJ*, 778, 188
- Valdes F., Gupta R., Rose J. A., Singh H. P., Bell D. J., 2004, *ApJS*, 152, 251
- van der Laan H., Perola G. C., 1969, *A&A*, 3, 468
- Wang J.-M., Chen Y.-M., Hu C., Mao W.-M., Zhang S., Bian W.-H., 2009, *ApJ*, 705, L76
- Yang X. et al., 2019, *ApJS*, 245, 17
- Zhang X.-G., Dultzin-Hacyan D., Wang T.-G., 2007, *MNRAS*, 377, 1215
- Zier C., 2005, *MNRAS*, 364, 583

This paper has been typeset from a  $\text{\TeX}/\text{\LaTeX}$  file prepared by the author.